Nature Communications

https://doi.org/10.1038/s41467-026-72844-4

Article in Press

E-cadherin inactivation shapes tumor microenvironment specificities in invasive lobular breast cancer

Received: 18 June 2025

Accepted: 27 April 2026

Cite this article as: Djerroudi, L., Mhaidly, R., Kieffer, Y. *et al.* E-cadherin inactivation shapes tumor microenvironment specificities in invasive lobular breast cancer. *Nat Commun* (2026). https://doi.org/10.1038/s41467-026-72844-4

Lounes Djerroudi, Rana Mhaidly, Yann Kieffer, Isabelle Damei, Hugo Croizer, Vithuzane Selvarasa, Geraldine Gentric, Laetitia Fuhrmann, Andreia Goncalves, Martial Caly, Camille Richardot, Renaud Leclere, Enora Laas, Caroline Malhaire, Kim Cao, Julia M. Houthuijzen, Pim Kloosterman, Jos Jonkers, Camille Benoist, Victor Renault, François-Clément Bidard, Anne Vincent-Salomon & Fatima Mechta-Grigoriou

E-cadherin inactivation shapes tumor microenvironment specificities in invasive lobular breast cancer

Lounes Djerroudi[1,2,3], Rana Mhaidly[1,2#], Yann Kieffer[1,2#], Isabelle Damei[1,2], Hugo Croizer[1,2], Vithuzane Selvarasa[1,2], Geraldine Gentric[1,2], Laetitia Fuhrmann[3], Andreia Goncalves[3], Martial Caly[3], Camille Richardot[3], Renaud Leclere[3], Enora Laas[4], Caroline Malhaire[5,6], Kim Cao[7], Julia M. Houthuijzen[8], Pim Kloosterman[8], Jos Jonkers[8], Camille Benoist[9], Victor Renault[9], François-Clément Bidard[10], Anne Vincent-Salomon[3,* &] and Fatima Mechta-Grigoriou[1,2,* &]

# These authors contributed equally

* These authors jointly supervised this work

[1] Institut Curie, Stress and Cancer Laboratory, Equipe labélisée par la Ligue Nationale contre le Cancer, PSL Research University, 26, rue d'Ulm, F-75248 Paris, France

[2] Inserm, U1339, 26, rue d'Ulm, Paris, F-75005, France

[3] Institut Curie, Institute of Women's Cancer, Department of Diagnostic and Theragnostic Medicine, 26, rue d'Ulm, F-75248 Paris, France

[4] Institut Curie, Institute of Women's Cancer, Department of Surgery, 26 rue d'Ulm, 75248 Paris Cedex 05, France

[5] Institut Curie, Institute of Women's Cancer, Department of Radiology, 26 rue d'Ulm, 75248 Paris Cedex 05, France

[6] Institut Curie, LITO Laboratory, INSERM U1288, Paris-Saclay University, 91401 Orsay, France

[7] Institut Curie, Institute of Women's Cancer, Department of Radiation Oncology, 26 rue d'Ulm, 75248 Paris Cedex 05, France

[8] Division of Molecular Pathology, Oncode Institute, The Netherlands Cancer Institute, Amsterdam, The Netherlands.

[9] Institut Curie, PSL University, Clinical Bioinformatics, 26 rue d'Ulm, 75248 Paris Cedex 05, France

[10] Institut Curie, Institute of Women's Cancer, Department of Medical Oncology, INSERM CIC 1428, Université Versailles Saint Quentin, 35 Rue Dailly 92210 Saint Cloud, France

[&] Corresponding: Fatima Mechta-Grigoriou E-mail address: fatima.mechta-grigoriou@curie.fr; Anne Vincent-Salomon Email address: anne.salomon@curie.fr.

ABSTRACT

Invasive lobular breast carcinoma (ILC) shows specific stromal features, and a high tumor-infiltrating lymphocyte (TIL) content being associated with poor patient prognosis. Here, we reveal the underlying mechanism by performing single-cell analysis, immunohistochemistry, deconvolution of bulk RNA-sequencing in a large female ILC series and functional assays. We show that E-cadherin (*CDH1)*-loss in breast cancer cells prevents differentiation of FAP+ inflammatory cancer-associated fibroblasts (iCAF) into FAP+ myofibroblastic CAF, leading to iCAF accumulation in ILC. In turn, FAP+ iCAF attract TILs into the tumor center, shaping their spatial organization. Subsequently, *CDH1*-inactivated ILC cancer cells promote immune escape through a lack of retention and activation of ITGAE-expressing resident memory CD8+ T lymphocytes (TRM). Hence, our study uncovers reciprocal interactions between *CDH1*-inactivated cancer cells, FAP+ iCAF and CD8+ TRM, providing insights into the ILC stromal reaction and revealing why and how TILs are associated with poor prognosis in ILC patients, a mechanism generalizable to other *CDH1*-inactivated cancer types.

INTRODUCTION

Invasive lobular carcinoma (ILC) is the second most common histological type of breast cancer, accounting for 5-15% of all breast carcinoma [1]. ILCs arise from the epithelial cells of the mammary ductal-terminal units, similar to invasive carcinomas of no special type (IC-NST) -the most common breast cancer subtype- but differ by a hallmark genetic driver event, the loss of CDH1/E-cadherin [2], which leads to the characteristic discohesive appearance of the lobular tumor cells. ILCs are mostly grade 2, estrogen receptor (ER)-positive and HER2-negative, whereas IC-NSTs display greater heterogeneity in terms of grade and molecular subtype; a difference that must be considered in comparative studies to avoid bias, particularly through appropriate matching for ER expression. ILCs encompass distinct histological forms: the classic histological type, composed of isolated or single-file monotonous epithelial cancer cells, is the most common one. The WHO classification [1] also defines histological variants based on tumor architecture (i.e., solid, alveolar) or cytology (i.e., pleomorphic, apocrine), which are often observed in combination. Clinically, patients with ILC exhibit specific characteristics [3] compared IC-NST, also known as invasive ductal carcinoma. Indeed, patients with ILC show older age of onset, larger tumor size at diagnosis, frequent multicentricity or bilaterality, more extensive lymph node involvement, a particular metastatic dissemination pattern [4, 5, 6], and a worse long-term prognosis than patients with IC-NST [6, 7, 8]. In addition, specific features of the tumor microenvironment have been identified by microscopic examination, including a minimal stromal reaction associated with a unique, nondestructive infiltration pattern of lobular cancer cells in the breast parenchyma and adipose tissue. More recently, stromal tumor-infiltrating lymphocytes (TILs) have also been associated with poor prognosis in ILC [9, 10]. To date, little is known about the link between these stromal features, the biological characteristics of lobular tumor cells and cancer-associated fibroblasts (CAF), the most abundant non-cancer cells of the tumor microenvironment.

In the last decade, CAF have been shown to be involved in almost all hallmarks of cancer, including extracellular matrix (ECM) remodeling, tumor invasion, immune regulation, resistance to treatment and metastatic spreading [11, 12, 13, 14, 15, 16]. CAF functions may depend on the tissue context and even more on the heterogeneity of their identity, as highlighted in pancreatic cancer [17, 18, 19, 20, 21], colon cancer [22], ovarian cancer [23], and in mouse and human breast cancer [11, 24, 25, 26, 27, 28, 29, 30]. Among these studies, our team identified four recurrent CAF populations (referred to as CAF-S1 to CAF-S4) across human cancers by performing integrated analyses of different CAF markers, including smooth muscle-alpha actin (SMA/ACTA2), Fibroblast Activation Protein (FAP), and Melanoma Cell Adhesion Molecule (MCAM), among others [11, 12, 23, 31, 32, 33, 34]. Interestingly,

both CAF-S1 (SMA+ FAP+ MCAM-) and CAF-S4 (SMA+ FAP- MCAM+) populations are pro-metastatic [12, 31]. Moreover, FAP+ CAF (CAF-S1) exhibit immunomodulatory functions by increasing the amount of regulatory CD4+ T lymphocytes [11, 25, 27, 35, 36, 37, 38, 39, 40, 41, 42] and by inhibiting CD8+ T cell cytotoxicity [34, 41, 43, 44, 45]. Subsequent single-cell RNA sequencing (scRNA-seq) analysis of FAP+ CAF revealed that this population is itself heterogeneous and composed of inflammatory and myofibroblastic CAF (FAP+ iCAF and FAP+ myCAF) in different cancer types, including IC-NST [27, 32, 33, 34], as previously identified in pancreatic cancer [17, 18, 19, 46, 47]. Indeed, FAP+ iCAF can be subdivided into two subgroups distinguished by expression of Anthrax toxin receptor 1 (ANTXR1): inflammatory FAP+ CAF (FAP+ iCAF, FAP+ ANTXR1-) composed of 3 clusters (Detox-iCAF, IL-iCAF, IFNγ-iCAF), and myofibroblastic FAP+ CAF (FAP+ myCAF, FAP+ ANTXR1+) composed of 4 main clusters (ECM-myCAF, characterized by high levels of Syndecan-1 [SDC1+], TGFβ-myCAF, Wound-myCAF, IFN$\alpha\beta$-myCAF). These clusters are characterized by distinct biological signatures with clinical relevance. Indeed, ECM-myCAF have been shown to be linked to resistance to immuno- and chemotherapies [27, 34].

To date, CAF heterogeneity has not yet been investigated in ILC, given that analyses have been mainly carried out on IC-NST. Data about CAF populations in ILC *versus* IC-NST remain very scarce, and only a few available studies consist mainly of single-marker immunohistochemical analyses [48, 49]. In addition, the impact of E-cadherin/*CDH1* loss in tumor cells on ILC stromal specificities remains largely unknown. In this context, we perform here an in-depth characterization of heterogeneity, functions and interactions of CAF populations with both immune and tumor cells in ILC, and compare them to IC-NST. To do so, we leverage a well-characterized retrospective series of 251 patients with ILC from Institut Curie, together with single-cell RNA sequencing (scRNA-seq) analysis from 6 ILC patients, and deconvolution of bulk RNA-seq data from large retrospective ILC and IC-NST series (N = 697) using an *in-house* integrated and annotated single-cell-based breast cancer cellular atlas. We find that ILCs accumulate more inflammatory FAP+ CAF / CAF-S1 (hereafter FAP+ iCAF) and less myofibroblastic FAP+ CAF / CAF-S1 (FAP+ myCAF) than ER+ IC-NSTs. Moreover, we uncover a mechanism by which E-cadherin/*CDH1* loss in cancer cells modulates FAP+ CAF plasticity and promotes specific accumulation of FAP+ iCAF in ILC. FAP+ iCAF enrichment promotes the attraction and accumulation of TILs and defines their spatial organization in ILC. In turn, *CDH1*-inactivated cancer cells maintain CD8+ TILs in a precursor state, decrease the content of ITGAE+ tissue-resident memory T cells (TRM) and thus promote the escape of ILC cancer cells from CD8+ T-cell cytotoxicity. Our study highlights the reciprocal interactions between *CDH1*-inactivated cancer cells, FAP+ iCAF, and CD8+ TRM and reveals the mechanism by which TILs are

associated with poor prognosis in patients with ILC, an effect that can be generalized to other *CDH1*-inactivated cancer types.

RESULTS

ILCs are enriched in inflammatory FAP+ CAF compared to IC-NSTs

In order to identify CAF populations in ILCs and compare their content with that in IC-NSTs, we first performed immunohistochemistry (IHC) on cases matched for ER status and compared ER+ cases in both ILCs (N = 158) and IC-NSTs (N = 77) series (see Supplementary Table 1 for clinico-pathological characteristics of the Curie retrospective series) using several CAF markers, including SMA, FAP, ANTXR1, SDC1, and MCAM (Fig. 1A-D, Supplementary Fig. 1A-C, and Supplementary Table 2 for a summary of available markers of CAF populations and FAP+ CAF clusters). Among the different CAF markers tested, we found that ILCs showed a significantly lower SMA histological score (H-score) compared to IC-NSTs (Fig. 1A, B and Supplementary Fig. 1A), suggesting ILCs contain fewer myofibroblastic populations than IC-NSTs. As SMA+ CAF include both FAP+ CAF (CAF-S1) and FAP- CAF (CAF-S4) populations, we assessed the expression of respective markers of each population, namely FAP and MCAM, which identify FAP+ CAF (CAF-S1) and FAP- MCAM+ CAF (CAF-S4), respectively. There was a tendency, although not significant (p=0.06), for a higher FAP H-score -and thus FAP+ CAF content- in IC-NSTs compared to ILCs (Fig. 1C). The proportion of MCAM+ cells was low in both IC-NSTs and ILCs (Supplementary Fig. 1B). In addition, SMA staining significantly correlated with FAP (Fig. 1C) but not with MCAM (Supplementary Fig. 1C), indicating that SMA+ CAF detected in ILCs are mainly FAP+ CAF (CAF-S1) and not FAP- MCAM+ CAF (CAF-S4). We then focused on FAP+ CAF cluster markers, *e.g.*, ANTXR1 enabling detection of myofibroblastic FAP+ CAF (FAP+ myCAF) clusters and SDC1, a specific marker of the ECM-myCAF cluster, one of the most abundant FAP+ myCAF clusters involved in immunotherapy resistance [27]. We found that ANTXR1 and SDC1 H-scores were significantly higher in IC-NSTs than in ILCs (Fig. 1D). H-scores of the different CAF markers analyzed were correlated (Pearson correlation coefficients between SMA and FAP H-scores: R=0.71, p<0.0001; between FAP and ANTXR1 H-scores: R=0.72, p<0.0001; and between ANTXR1 and SDC1 H-scores: R=0.52, p<0.0001). We then combined the analysis of these single markers to evaluate more precisely the content of the different FAP+ CAF clusters. We focused our analysis on tumors enriched in FAP+ CAF (FAP H-score > 1st quartile) and stratified cases according to ANTXR1 and SDC1 H-scores: FAP+ iCAF-enriched cases were defined as $ANTXR1^{Low}$, ECM-myCAF-enriched cases as $ANTXR1^{High}$ $SDC1^{High}$, and cases enriched in other myCAF clusters as $ANTXR1^{High}$ $SDC1^{Low}$ (see also Methods *#Immunostaining* for determination of the thresholds by Gaussian mixture models). Using this combined analysis, we found that ILCs were enriched in FAP+ iCAF and had less ECM-myCAF compared to IC-NSTs

(Fig. 1E). Since IC-NSTs had a higher proportion of grade 3 tumors than ILCs, we next investigated whether the differences observed in FAP+ CAF cluster content between ILCs and IC-NSTs could be confounded by grade. When we restricted our analysis to grade 1-2 ILCs and IC-NSTs, a comparison of H-scores of CAF markers confirmed enrichment in FAP+ iCAF and depletion in ECM-myCAF in ILCs compared to IC-NSTs (Supplementary Fig. 1D, E).

To investigate the differences in FAP+ CAF cluster content between ILCs and IC-NSTs at higher resolution, we performed single-cell RNA sequencing (scRNA-seq) analysis of 6 ER+ ILC patients (Supplementary Table 3 for clinico-pathological characteristics of the prospective scRNA-seq ILC cohort), and compared these ILC data with publicly available scRNA-seq datasets from 36 IC-NSTs and 8 normal breast samples [33, 41, 50, 51]. To do so, we first integrated all these scRNA-seq datasets and established a cellular atlas composed of 109,137 cells including 35,995 cells from ER+ ILCs and 29,426 cells from ER+ IC-NSTs, as well as 34,835 cells from non-luminal IC-NSTs and 8,881 normal fibroblasts, encompassing 47 different cell types and cell states (ILC & IC-NST single-cell Atlas, Supplementary Fig. 2A, B; see also Methods, #Building a reference lobular and ductal single-cell RNA-seq atlas). This scRNA-seq-based cellular atlas showed extensive mixing of cells from different patients within stromal, lymphoid, myeloid, and endothelial populations (Supplementary Fig. 2C), indicating that the cell-type annotations were consistent across samples and not driven by a patient-specific bias. Although this atlas provides high-resolution cell-type definitions, a few sub-populations are closely related, which may introduce uncertainty in bulk RNA-seq deconvolution. However, expression of canonical markers indicated that these clusters are biologically distinct (Supplementary Fig. 2D), supporting the chosen granularity. In this ILC & IC-NST single cell Atlas, seven FAP+ CAF clusters (Detox-iCAF, IL-iCAF, IFNγ-iCAF, ECM-myCAF, TGFβ-myCAF, Wound-myCAF, IFN$\alpha\beta$-myCAF) were detected, as recently reported [27]. UMAP representation of FAP+ CAF clusters according to breast cancer histological types confirmed FAP+ iCAF enrichment (in particular the Detox-iCAF and IL-iCAF clusters) and myCAF depletion (in particular the ECM-myCAF cluster) in ILCs compared to IC-NSTs (Fig. 1F). As the number of tumors studied by scRNA-seq was limited, we next sought to explore the content of FAP+ CAF clusters in larger ILC and IC-NST cohorts at a single-cell-like resolution. To do so, by using our ILC & IC-NST single cell Atlas and the BayesPrism algorithm, we deconvoluted bulk RNA-seq data from the Institut Curie retrospective ILC series (N=251 cases) (Supplementary Table 4 for clinico-pathological characteristics of the retrospective ILC series analyzed by bulk RNA-seq), as well as IC-NSTs from the TCGA (N=446 cases) and IC-NSTs from the Institut Curie SCANDARE cohort (N=78 cases) [52] (see Methods, *#Deconvolution of bulk RNA-seq data*). This analysis confirmed the higher content in FAP+ iCAF, in particular

Detox-iCAF, and the lower proportion of ECM-myCAF in ILCs compared to IC-NSTs (Fig. 1G). Of note, deconvolution analysis of each individual case from the retrospective Curie series revealed a high degree of heterogeneity in the proportion of FAP+ CAF clusters across ILCs (Fig. 1H). To determine whether this FAP+ CAF cluster heterogeneity could be related to the histopathological features of ILCs, we performed an unsupervised clustering of the retrospective Curie series based on the proportion of FAP+ CAF clusters among all FAP+ CAF. Interestingly, we found that the histological subtype (classic / non-classic) and tumor cellularity (high / low) were associated with an enrichment in specific FAP+ CAF clusters (Fig. 1I and Supplementary Fig. 1F). In particular, low ECM-myCAF content and high Detox-iCAF content were associated with the classic ILC subtype and low cancer cell cellularity (Fig. 1I). These results (high Detox-iCAF and low ECM-myCAF content in classic ILC with low cancer cell cellularity) were confirmed by the combined IHC analysis of FAP+ CAF cluster markers (Fig. 1J). Finally, we compared the CAF landscape in ILC mouse models harboring the genetic background found in classic ILC (CDH1/PIK3CA and CDH1/PTEN) (Fig. 1K). As detected in patients, we observed a significant accumulation of iCAF in *CDH1*-mutated ILC mouse models compared to control mice (Fig. 1K), providing functional *in vivo* evidence that CDH1 mutation promotes an iCAF-enriched tumor microenvironment. Taken together, these data demonstrate that ILCs contain a significantly higher proportion of FAP+ iCAF and a lower content of the ECM-myCAF cluster than IC-NSTs.

CDH1/E-cadherin loss in lobular cancer cells prevents differentiation of Detox-iCAF into ECM-myCAF, leading to FAP+ iCAF accumulation

We next sought to uncover the mechanism driving FAP+ iCAF accumulation and reducing ECM-myCAF content in ILCs. Recently, we showed that, upon contact with cancer cells, FAP+ iCAF differentiate into FAP+ myCAF via a trajectory from Detox-iCAF to ECM-myCAF [33]. Since E-cadherin/*CDH1* loss is a hallmark of ILC cancer cells, we wondered whether *CDH1* inactivation might directly impact differentiation of FAP+ CAF clusters in contact with cancer cells. We first performed *in silico* analyses by applying the CellChat algorithm to our ILC & IC-NST single-cell Atlas in order to infer ligand-receptor (L-R) interactions and predict cell-to-cell communications, with a particular focus on cancer cells and FAP+ CAF clusters. When considering all signaling pathways, global L-R analysis revealed that FAP+ CAF clusters were the main senders of L-R signals in both ILCs and IC-NSTs (Fig. 2A), reinforcing their relevance in breast cancer biology. L-R analysis focused on the E-cadherin pathway demonstrated that FAP+ CAF clusters were the cells that received the most E-cadherin-mediated signals from ductal cancer cells in IC-NSTs (Fig. 2B), suggesting that E-cadherin-dependent crosstalk between cancer cells and FAP+ CAF

clusters might be key in FAP+ CAF cluster differentiation. Contribution analysis revealed that Integrin-β1/ITGB1 was the dominant contributor to the CDH1 signaling pathway. Moreover, ITGB1 was one of the E-cadherin receptors expressed at high levels in FAP+ CAF clusters and showed one of the most significant interactions with E-cadherin+ cancer cells ($p < 0.01$) in IC-NSTs (Fig. 2C and Supplementary Fig. 3A). As expected, these interactions were not detected in ILCs, where cancer cells are mutated in *CDH1*, while *ITGB1* remains highly expressed in ILC FAP+ CAF clusters (Supplementary Fig. 3A). To assess the impact of E-cadherin pathway inactivation on FAP+ CAF plasticity, we performed *in vitro* functional assays. To this end, we established primary cultures of FAP+ iCAF from breast cancer, as previously done in [27, 33] (see also Methods, *#Isolation and characterization of primary FAP+ CAF / CAF-S1 clusters for functional assays*) and co-cultured them with ER+ breast cancer cell lines (MCF7 and T47D) silenced or not for *CDH1* (Supplementary Fig. 3B). Notably, we chose to use FAP+ iCAF cells instead of normal fibroblasts for co-culture experiments, as human normal fibroblasts are difficult to maintain in a normal-like state *in vitro,* FAP expression being stimulated under most culture conditions [11]. The FAP+ CAF cluster composition at baseline and after co-culture with cancer cells was determined by FACS using a combination of markers as previously published [27, 33]. While FAP+ CAF clusters were mainly composed of ANTXR1- FAP+ iCAF before co-culture, the percentages of ANTXR1+ FAP+ myCAF reached almost 40% in the presence of E-cadherin+ ER+ cancer cells (Fig. 2D, E and Supplementary Fig. 3C). Interestingly, this effect was totally abrogated upon co-culture with ER+ cancer cells silenced for *CDH1* (Fig. 2D, E and Supplementary Fig. 3B, C). The analysis of additional markers of FAP+ CAF clusters confirmed that, before co-culture, FAP+ iCAF were predominantly represented by Detox-iCAF, with less than 10% ECM-myCAF (Fig. 2E and Supplementary Fig. 3C). After co-culture with MCF7 or T47D (siCTRL condition), there was a significant increase in the percentage of ECM-myCAF at the expense of Detox-iCAF, while the proportion of the other clusters did not change (Fig. 2E and Supplementary Fig. 3C), confirming our recent observations in IC-NST [33]. Interestingly, the plasticity between FAP+ CAF clusters (from Detox-iCAF to ECM-myCAF) was completely abolished by *CDH1* silencing (siCDH1 condition) in the two cancer cell lines analyzed (Fig. 2E and Supplementary Fig. 3C). We confirmed that co-culture of iCAF with the ILC cancer cell line SUM44PE, characterized by E-cadherin loss, did not convert iCAF into myCAF (Supplementary Fig. 3D). In addition, co-culture of FAP+ myCAF with ER+ cancer cells silenced or not for *CDH1* had no effect on myCAF (Supplementary Fig. 3E), suggesting that CDH1 does not modulate reprogramming of FAP+ myCAF into iCAF. As we identified ITGB1 as the receptor at the surface of FAP+ CAF that might be involved in the E-cadherin-dependent crosstalk with cancer cells, we silenced *ITGB1* in FAP+ iCAF and tested its

effect on FAP+ iCAF plasticity (Fig. 2F, G and Supplementary Fig. 4A, B). Inactivation of *ITGB1* in FAP+ iCAF prevented their transition toward ANTXR1+ FAP+ myCAF, in particular into the ECM-myCAF cluster upon co-culture with E-cadherin+ ER+ breast cancer cells (Fig. 2F, G and Supplementary Fig. 4B). Thus, these results show that E-cadherin loss in ILC breast cancer cells prevents Detox-iCAF differentiation into ECM-myCAF, potentially via lack of interaction with *ITGB1*. This explains, at least in part, the accumulation of FAP+ iCAF at the expense of ECM-myCAF in ILC compared to IC-NST patients.

FAP+ iCAF shape the spatial organization of TILs in ILCs

Given that FAP+ CAF (CAF-S1) can interact with TILs [11, 23, 27, 33, 34], we explored the impact of FAP+ CAF clusters on the content and spatial organization of TILs in ILCs. Among the 251 ILC cases of the Curie retrospective cohort, 72.5% of ILCs (182 cases) showed less than 5% (< 5%) TILs and only 27.5% of ILCs (69 cases) exhibited more than 5% (≥ 5%) TILs. A high percentage of TILs (≥ 5%) correlated significantly with high grade ($p < 0.01$) and non-luminal phenotype ($p < 0.01$). Analysis of cases with detected TILs (206 cases with TILs > 0% among 251 total ILC) showed two types of TIL spatial organization: an infiltrating pattern in 62% of ILCs (128 cases among 206 ILC) and a margin-predominant pattern in 38% of ILCs (78 cases among 206 ILC) (Fig. 3A). The margin-predominant TIL pattern correlated with increased tumor cellularity ($p < 0.05$). There was no association between the TIL organization pattern and any of the other clinicopathological variables (age, grade, pT, pN, histomolecular class, lympho-vascular invasion and total percentage of TILs).

Based on these first observations, we next studied the associations between the percentages and spatial organization of TILs and the content of FAP+ CAF clusters assessed by IHC. For all following analyses, similar data were obtained when analyses were performed on total ILC or when restricted to ER+ ILC. ER+ ILCs with high TIL percentages (≥5%) had significantly higher FAP and ANTXR1 H-scores than ER+ ILCs with low TILs (<5%) (Supplementary Fig. 5A), even after adjustment for grade (Supplementary Fig. 5B), suggesting a higher FAP+ CAF content in TIL-enriched ILCs. As we did not observe major differences in total TIL content according to FAP+ CAF clusters (Supplementary Fig. 5C), we analyzed the link between spatial organization of TILs and FAP+ CAF clusters (Fig. 3A-D and Supplementary Fig. 5D, E). We found that ER+ ILCs with infiltrated TILs showed significantly lower levels of all FAP+ CAF markers (SMA, FAP, ANTXR1, SDC1) than cases with margin-predominant pattern (Fig. 3B). In agreement with this, combined analysis of these markers revealed that cases with infiltrating TIL pattern were significantly enriched in FAP+ iCAF, while cases with margin-predominant

pattern were enriched in ECM-myCAF (Fig. 3C). We confirmed these observations by performing spatial transcriptomics on infiltrating and margin-predominant TIL patterns (Supplementary Fig. 5F, G). Since high tumor cellularity was associated with both margin-predominant pattern and high ECM-myCAF content, we wanted to exclude this potential confounding factor. We then restricted the analysis to cases with high tumor cellularity (≥50%) and confirmed higher SMA, FAP, ANTXR1 and SDC1 protein levels in margin-predominant than in TIL infiltrating ER+ ILCs (Supplementary Fig. 5D). Consistent with these observations, combined analysis of all these FAP+ CAF markers showed an accumulation of the ECM-myCAF cluster in margin-predominant ILCs and an enrichment of FAP+ iCAF in TIL-infiltrating ER+ ILCs (Supplementary Fig. 5E). These results were confirmed by performing deconvolution of bulk RNA-seq from the ER+ ILC retrospective series using the ILC & IC-NST cellular Atlas (Fig. 3D). Indeed, quantitative analyses assessing the proportion of one cell type relative to all others confirmed that ER+ ILCs with the TIL infiltrating pattern were enriched in FAP+ iCAF clusters (mainly Detox-iCAF), in agreement with the enrichment in cytokines detected in the signature of FAP+ iCAF (Supplementary Data 1). In contrast, ER+ ILCs with the margin-predominant pattern were characterized by high content of FAP+ myCAF, in particular ECM-myCAF, supporting IHC data (Fig. 3D). Altogether, these observations based on ILC patient samples show strong associations between specific FAP+ CAF clusters and TIL spatial organization, without affecting total TIL content.

Based on the association between FAP+ CAF clusters and TIL spatial distribution, we next sought to validate the impact of FAP+ CAF clusters on TIL migration by performing transwell migration assays. As CD8+ T lymphocytes are key TIL components, we compared the ability of FAP+ iCAF and ECM-myCAF to attract CD8+ T lymphocytes *in vitro* (Fig. 3E, F). To have a more complete view of ILC tumors, we also analyzed the capacity of ER+ breast cancer cells (MCF7 or T47D) silenced or not for *CDH1* to attract CD8+ T cells (Fig. 3E, F). These functional migration assays showed that only FAP+ iCAF had the ability to strongly attract CD8+ T lymphocytes, while ECM-myCAF and E-cadherin+ or E-cadherin– cancer cells had no or only a weak attraction effect (Fig. 3E, F). Co-culture of breast cancer cells (MCF7 or T47D) with FAP+ iCAF totally abolished CD8+ T cell migration (Fig. 3E, F), consistent with the transition of FAP+ iCAF towards ECM-myCAF in the presence of E-cadherin+ cancer cells. Interestingly, silencing of *CDH1* in cancer cells restored CD8+ T cell attraction by FAP+ iCAF (Fig. 3E, F), thereby confirming that FAP+ iCAF were able to attract CD8+ T lymphocytes, while FAP+ myCAF were not. Similar results were obtained when cancer cells were co-cultured with FAP+ iCAF silenced for *ITGB1*, thereby highlighting the involvement of the E-cadherin-ITGB1-dependent pathway in FAP+ iCAF plasticity and CD8+ TIL attraction (Fig. 3G, H). Taken together, these data are consistent with FAP+ iCAF

being associated with TIL infiltration and ECM-myCAF with *in situ* immune exclusion in ILC patients. These data also highlight the impact of *CDH1* inactivation on FAP+ iCAF identity and TIL organization pattern.

TIL content and spatial organization are associated with poor prognosis in patients with ILC

We next investigated the impact of FAP+ CAF cluster content, TIL infiltration and their spatial distribution on the survival of ILC patients. While enrichment of FAP+ CAF clusters in ILC was not associated with risk of mortality (overall survival, OS or breast cancer-specific survival, BCSS) or with risk of metastasis (distant metastasis-free interval, DMFI) (Supplementary Fig. 5H), the content and spatial organization of TILs (classified into four subgroups: TILs <5% margin-predominant, TILs <5% infiltrating, TILs ≥5% margin-predominant, TILs ≥5% infiltrating) had a significant prognostic value (Fig. 4A). Survival curves showed that ILC patients with the worst survival (BCSS and OS and the highest DMFI risk) were suffering from ILCs with both ≥5% TILs and an infiltrating TIL organization pattern (global log-rank test < 0.05 for OS 0.07 for BCSS, and < 0.05 for DMFI; pairwise log-rank test < 0.05 for OS, BCSS and DMFI for comparison of this group with TILs <5% margin-predominant cases) (Fig. 4A). Cox analysis of OS and DMFI showed that the ILC subgroups with an infiltrating TIL pattern were significantly associated with a poor prognosis (in both OS and DMFI) and had a higher hazard ratio (HR) than subgroups with a margin-predominant pattern (Fig. 4B). This confirms our previous observations on the negative impact of TILs on ILC patient survival [10] but also goes a step further by highlighting the impact of TIL spatial distribution on ILC patient prognosis.

Other characteristics significantly associated with survival in univariate analysis were age (OS), grade (DMFI), lympho-vascular invasion (OS), PR status (BCSS and OS), pT and pN (DMFI, BCSS and OS) and *CDH1* mutational status (DMFI) (Supplementary Table 5). Multivariate analysis showed that the content and spatial organization of TILs retained their prognostic value independently of all other variables (Fig. 4C). Indeed, the TILs ≥5% infiltrating subgroup was the one associated with the worst prognosis among the four TIL-based ILC subgroups (HR 8.16 [95% CI 1.61–41.4] for OS; HR 8.4 [95% CI 1.61–43.8] for DMFI) (Fig. 4C). This TILs ≥5% infiltrating subgroup also had a higher HR compared with the TILs ≥5% margin-predominant subgroup (HR 3.15 [95% CI 0.55–17.9] for OS; HR 4.58 [95% CI 0.81–26] for DMFI). Of note, the TILs ≥5% infiltrating group did not have a statistically different global TIL content compared to the TILs ≥5% margin-predominant group (10.11% versus 7.73% respectively, p = 0.67) but did have a significantly higher amount of intratumor TILs (10% vs. 4.7% respectively, p = 0.02).

We next aimed to investigate by unsupervised analyses if TIL-related organization and prognosis in ILC patients could be related to the content of any other cellular components in the tumor, in particular FAP+ iCAF and ECM-myCAF. Unsupervised clustering built on the deconvolution of bulk RNA-seq data from the ILC retrospective cohort enabled us to identify 4 ILC subgroups based on TME components shared across patients. These 4 TME classes (called "TEDI TME classes" based on the first letter of the FAP+ CAF component in each class) were associated with distinct clinico-pathological features and prognoses: TME class 1 (TGFβ/Wound-myCAF-enriched), TME class 2 (ECM/IFNαβ-myCAF-enriched), TME class 3 (Detox-iCAF-enriched) and TME class 4 (Immune cell-enriched). (Fig. 4D). The ILC TME class 1 subgroup showed a high proportion of normal epithelial and myoepithelial cells, high content in TGFβ-myCAF and Wound-myCAF, and a low overall quantity of TILs with nevertheless a high fraction of naïve CD4+ T cells. The ILC TME class 2, enriched in margin-predominant TIL pattern and non-classic ILC, showed a high proportion of FAP+ myCAF, including ECM-myCAF and IFNαβ-myCAF, as well as tumor cells, TREM2+ tumor-associated macrophages (TAM), SPP1+ TAM and CD16+ monocytes. The ILC TME class 3, enriched in classic ILC, was characterized by low tumor cellularity associated with high fractions of Detox-iCAF, endothelial cells, cancer-associated pericyte-like cells and NK-NKG2A cells. Finally, the ILC TME class 4, characterized by high IFNγ-iCAF content, showed a high proportion of ILC with abnormal but remaining E-cadherin IHC expression, and was enriched in TILs, including GZMH+ and GZMK+ CD8+ T lymphocytes, IL7R+ CD4+ memory T lymphocytes and FOXP3+ Tregs (Fig. 4D). Of note, no significant association was found between *CDH1* mutational status and ILC subgroups, or with FAP+ CAF or CD8+ T cell subpopulations. Consistent with the negative impact of TILs on ILC patient survival, the TME class 4 exhibited the worst prognosis and the TME class 1 showed an excellent prognosis (Supplementary Fig. 5I). Interestingly, the identified clusters are an independent prognostic factor from usual clinicopathological features (age, grade, pT, pN, LVI, hormone receptors, percentage of TILs, *CDH1* mutational status) for overall survival in multivariate analysis (Supplementary Fig. 5J). In conclusion, FAP+ iCAF are associated with an infiltrating intratumoral TIL pattern, which itself predicts a poor prognosis in ILC patients, in contrast to what is usually observed in most cancers.

CDH1/E-cadherin loss induces immune escape by preventing retention and activity of ITGAE-expressing resident memory CD8+ T cells

As global TIL content predicts poor prognosis in ILC patients [9, 10], we next investigated the mechanism that might impair the anti-tumor activity of specific immune cell populations against

lobular tumor cells. We focused our study on CD8+ T lymphocytes, given their well-established role as key effectors in anti-tumor immunity [53, 54, 55], and because previous studies have raised questions regarding their functional impact in the context of ILC [9, 56]. As the overall CD8+ T lymphocyte content was similar between ER+ ILCs and IC-NSTs (Supplementary Fig. 6A), we checked if we could identify different CD8+ T cell states in these two histological types by comparing CD8+ T cell scRNA-seq data in ER+ ILCs *versus* IC-NSTs. In total, 15,605 high-quality CD8+ T lymphocytes were present in our ILC & IC-NST single-cell Atlas, including 10,919 CD8+ T lymphocytes from ILCs and 4,686 from IC-NSTs. Five CD8+ T cell clusters [57] were identified and annotated via label transfer (see Methods, #Building a reference lobular and ductal single-cell RNA-seq atlas): three precursor CD8+ T cell clusters (referred to as CD8-KLF2, CD8-GZMK and CD8-XCL1), a transitional CD8+ T cell cluster (CD8-GZMH), and a mature cytotoxic CD8+ T cell cluster (CD8-FCGR3A) (Fig. 5A). Comparative quantification of CD8+ T lymphocyte clusters (relative to total CD8+ T cell content) between ER+ ILCs and ER+ IC-NSTs showed a significant enrichment of CD8-KLF2 precursors (54% vs 11%) in ILCs, together with a reduced content of CD8-GZMK cells (6.6% vs 48%) and an almost complete depletion of the transitional CD8-GZMH cluster (0.74% vs 17%) ($p < 0.001$) (Fig. 5B). Interestingly, the CD8-GZMH cluster, almost completely depleted in ILCs compared to IC-NSTs, expressed ITGAE (also known as CD103) (Fig. 5C), a receptor known to interact with E-cadherin and to be involved in the formation of the immunological synapse [58]. L-R analysis based on the CDH1-ITGAE (E-cadherin-CD103) interaction showed an exclusive interplay between CD8-GZMH and IC-NST cancer cells (Supplementary Fig. 6B). It is noteworthy that CD8+ T lymphocytes were the only T-cell subpopulation found to interact with tumor cells via the *CDH1* pathway in IC-NST; no such interaction was observed with CD4+ T lymphocytes or with macrophages (Supplementary Fig. 6B), thereby supporting the potential role of the E-cadherin-mediated pathway on CD8+ T lymphocytes. Regarding *CDH1*-mutated ILC cancer cells, no interaction was found with CD8-GZMH via the CDH1-ITGAE (E-cadherin-CD103) receptors (Supplementary Fig. 6B), suggesting that inactivation of the E-cadherin-dependent pathway might be key in depletion of the CD8-GZMH T-cell cluster in ILCs. In addition, applying a signature from [55] demonstrated that the CD8-GZMH population actually corresponded to the well-described resident memory CD8+ T lymphocytes (TRM) (Fig. 5D), a population with strong antitumor and cytotoxic properties [55, 58, 59, 60, 61, 62], which has been shown to be reduced when E-cadherin expression is lost [63]. Regulation of the resident memory phenotype is known to notably involve the *KLF2* gene [64]. This could be linked to the anti-correlation we found between expression of *KLF2* and *ITGAE* in CD8+ T lymphocytes in our single-cell atlas (Supplementary Fig. 6C), as well as to the enrichment of the

CD8-KLF2 population in ILCs concomitant with the depletion of the CD8-GZMH TRM cluster (as shown in Fig. 5B).

We next aimed to validate these scRNA-seq data, in particular the decrease in ITGAE+ TRM content, in a large cohort of ILC patients. To do so, we analyzed the different clusters of CD8+ T lymphocytes by deconvoluting bulk RNA-seq from the Curie retrospective ER+ ILC series and from the ER+ TCGA IC-NSTs series. We selected cases where at least 5% of lymphoid cells were detected in order to characterize cases that were the most enriched in TILs and with sufficient signal to be interpreted. The analysis confirmed the enrichment of the CD8-KLF2 cluster and the depletion of both CD8-GZMK and CD8-GZMH TRM clusters in ILCs compared to IC-NSTs (Fig. 5E). In addition, the ratio of CD8-GZMH TRM to CD8-KLF2 content was significantly lower in ER+ ILCs than in IC-NSTs (Fig. 5F). Of note, the CD8-GZMH/CD8-KLF2 ratio had no impact on survival in ILC (OS: HR = 1.31, 95% CI 0.88–1.95, p = 0.19), even when analyses were stratified by E-cadherin status. An IHC analysis was then performed to compare the content of ITGAE/CD103+ immune cells (mainly represented by CD8+ TRMs in cancer [65, 66, 67, 68, 69]) in ER+ IC-NSTs *versus* ILCs. We investigated whether the ITGAE/CD103+ T-cell content could vary with the histo-phenotypic characteristics of ILCs. We did not detect any link with FAP+ CAF cluster content. We then tested if *CDH1* inactivation in cancer cells could be associated with the lack of ITGAE/CD103+ CD8+ TRM in ILC. *CDH1* genetic alterations in ILC lead phenotypically either to a complete absence of E-cadherin expression, or to an abnormal (incomplete membrane staining with reduced intensity) E-cadherin staining. Interestingly, E-cadherin-negative ILCs had a significantly lower content of ITGAE/CD103+ T lymphocytes compared to ILCs displaying abnormal E-cadherin expression (Supplementary Fig. 6D). In addition, ILCs of the classic subtype also had a lower content of ITGAE/CD103+ T lymphocytes than non-classic ILCs (Supplementary Fig. 6E). Of note, there was no correlation between grade and ITGAE/CD103+ T cell content in either ILCs or IC-NSTs (Supplementary Fig. 6F). Overall, classic E-cadherin-negative ILCs (the typical form of ILC) contained significantly fewer ITGAE/CD103+ T lymphocytes than IC-NSTs (Fig. 5G), while the total number of CD8+ T lymphocytes remained similar between these two tumor types (Supplementary Fig. 6G).

As we observed a significant depletion of CD8+ TRM in ILCs, we finally tested the consequences of *CDH1* inactivation on CD8+ T cell cytotoxic activity and IFNγ secretion by performing functional assays. Co-culture of ITGAE/CD103+ CD8+ T lymphocytes with E-cadherin+ breast cancer cell lines (MCF7 or T47D) significantly increased the expression of IFNγ, Perforin, GZMK and GZMB (Fig. 5H, I and Supplementary Fig. 6H, I), reflecting increased CD8+ T cell cytotoxicity and activation. Interestingly, *CDH1* silencing in cancer cells prevented this

ITGAE/CD103+ CD8+ T cell cytotoxic response (Fig. 5H, I and Supplementary Fig. 6H, I). In contrast to ITGAE/CD103+ CD8+ T cells, co-culture of ITGAE/CD103- CD8+ T lymphocytes with E-cadherin+ breast cancer cells prevented IFNγ secretion and expression of cytotoxic markers, highlighting the required expression of both E-cadherin in cancer cells and ITGAE/CD103 in CD8+ T lymphocytes to induce a cytotoxic response. We then investigated the generalizability of this mechanism, by analyzing scRNA-Seq data from gastric cancer [70]. We observed consistent results confirming accumulation of specific clusters of inflammatory FAP+ CAF and precursors of CD8+ T lymphocytes in the diffuse gastric cancer subtype, characterized by E-cadherin/*CDH1* alteration. Specifically, the diffuse type of gastric cancers exhibited a higher proportion of iCAF, particularly IL-iCAF (Fig. 5J). This subtype also showed an enriched fraction of CD8-KLF2 and CD8-XCL1 T cell populations, accompanied by a concomitant depletion of CD8-GZMH and CD8-GZMK populations (Fig. 5K, L). Consistently, we found a decrease in the expression of a CD8+ TRM-specific signature in the diffuse-subtype compared to the intestinal one (Fig. 5L). In conclusion, loss of *CDH1* in ILC could constitute an immune escape mechanism through lack of interaction of E-cadherin– cancer cells with ITGAE/CD103-expressing resident memory CD8+ T cells, leading to impaired retention and activation of CD8+ T lymphocytes. These observations can be extrapolated to other *CDH1*-inactivated cancer types, such as the diffuse gastric cancer subtype.

DISCUSSION

Most comprehensive studies of the tumor microenvironment in breast cancer to date have not taken histological type into account. ILC is a well-established histomolecular entity, with features distinct from IC-NST [3, 71]. The stromal specificities of ILC, recognized by pathologists for several decades, have so far received no biological explanation. In addition, the impact of E-cadherin/*CDH1* loss (the hallmark of lobular tumors) on ILC stroma has never been explored. Leveraging previous high-resolution characterization of CAF populations in IC-NST [11, 12, 24, 26, 27, 31, 72], we investigated CAF heterogeneity in ILC, particularly FAP+ CAF (also called CAF-S1), a major stromal population with immunomodulatory properties. To this end, we combined immunohistochemistry, transcriptomic analysis, single-cell RNA seq, as well as functional experiments. We established a comprehensive breast cancer cellular atlas based on lobular and ductal breast cancer scRNA-seq data, which allowed us to deconvolute bulk RNA-seq data and characterize large ILC and IC-NST series at the cell-type and cell-state-scale resolution. All our analyses converge to demonstrate the dual impact of E-cadherin*/CDH1* loss in cancer cells on both CAF plasticity and CD8+ T-cell immune escape (Fig. 6A).

Comparative analysis of CAF populations reveals a lower myofibroblastic content (SMA^{+}) in ILCs than in ER+ IC-NSTs, associated with enrichment of FAP+ iCAF (SMA^{Low} FAP^{+} $ANTXR1^{-}$) and depletion of FAP+ myCAF (SMA^{High} FAP^{+} $ANTXR1^{+}$), particularly in the ECM-myCAF ($SDC1^{+}$) cluster. This finding is consistent with microscopic observations showing a poorly activated stroma in ILCs, which sometimes makes histopathological identification of ILCs difficult [1]. Here, we also identify the mechanism underlying this enrichment in FAP+ iCAF content. Indeed, we demonstrate that the E-cadherin-dependent pathway is involved in CAF differentiation, in particular in the transition of inflammatory towards myofibroblastic FAP+ CAF. This process involves E-cadherin expressed by cancer cells and ITGB1 receptor expressed by FAP+ CAF, suggesting heterologous interactions between these two proteins which have previously been described in other contexts [73, 74]. This mechanism involved in the iCAF-to-myCAF transition was supported both by *in silico* ligand-receptor analyses of scRNA-seq data and by functional evidence from co-culture experiments between breast cancer cell lines and FAP+ iCAF [18, 33, 46]. It should be noticed that other integrins ($\alpha v\beta 6$ and $\alpha v\beta 8$) have already been shown to be involved in fibroblast activation, notably through activation of latent forms of TGFβ1 and TGFβ3 [75, 76, 77], but no E-cadherin-mediated integrin involvement has yet been described. Beyond ILC, E-cadherin downregulation occurring in other cancers and/or in other contexts (i.e. *CDH1* methylation, epithelial-mesenchymal transition…) could also significantly impact stromal composition, as we

show here in gastric cancers. Furthermore, the role of the E-cadherin-dependent pathway in fibrosing diseases, which can be triggered or maintained by alterations in epithelial cells [77], remains to be determined. In this context, inflammatory fibroblasts have recently been identified in early stages of chronic kidney disease [32]. Despite being overall depleted in myofibroblasts and FAP+ myCAF, certain ILC cases exhibit a high IHC staining for SMA, ANTXR1, and SDC1 CAF cluster markers, in line with enrichment of ECM-myCAF in a few patients, an observation confirmed by deconvolution analyses. These observations suggest E-cadherin-independent mechanisms of myCAF differentiation in ILCs, which may involve the TGFβ pathway as demonstrated in other cancers [19, 33, 46, 78, 79, 80]. Interestingly, we found that heterogeneity of CAF composition was associated with histopathological heterogeneity of ILCs. Notably, enrichment in myCAF, and especially ECM-myCAF, was greater in ILCs with high tumor cellularity and in the non-classic ILC histological subtype, characterized by specific tumor architecture. These two features may reflect particular mechanical stresses, which could promote fibroblast activation (potentially through YAP/TAZ), as recently shown in pancreatic and ovarian cancer, as well as in IC-NST [33, 34, 81, 82]. Further characterization of non-classic ILC may be required to identify the factors involved in ECM-myCAF accumulation in these ILC patients.

Interestingly, we observe that the content of the different FAP+ CAF clusters has an impact on TIL spatial organization. ECM-myCAF are associated with a margin-predominant TIL organization pattern, suggesting that this FAP+ CAF cluster may promote immune exclusion through an ECM-mediated physical barrier, as previously shown [43, 83, 84, 85]. In turn, FAP+ iCAF content correlates with an infiltrating TIL pattern (significant association for Detox-iCAF and IL-iCAF). These observations in cancer tissues are supported by functional analyses showing the exclusive ability of FAP+ iCAF to significantly attract lymphocytes *in vitro*, consistent with the known properties of inflammatory CAF to secrete high levels of chemoattractant cytokines and chemokines [14, 27, 32, 33, 34, 81] (See Supplementary Data 1 for gene signatures). Furthermore, the functional experiments show that silencing the E-cadherin heterologous receptor expressed in CAF might promote the penetration of TILs into the tumor core (via iCAF accumulation) and reduce the accumulation of immunosuppressive FAP+ myCAF involved in resistance to immunotherapy [27]. We also demonstrate that the spatial organization of TILs, in addition to the global TIL amount, is an independent prognostic factor in multivariate analysis. Cases with an infiltrative TIL pattern have a worse prognosis (in terms of metastatic risk and mortality) than cases with margin-predominant TILs, supporting, through this qualitative spatial TIL analysis, the previously described quantitative association between TILs and poor prognosis in ILC [9, 10]. It has been previously shown that this could partially be due to M2-like macrophage enrichment and to

CD8+ T-cell restriction in stroma [9, 56], the latter being consistent with FAP+ iCAF enrichment in ILC stroma and their strong attractive properties. Here, we show in addition that the poor prognostic value of TILs could be -at least in part- explained by a specific profile of CD8+ T-cell infiltrate in ILC, especially depleted in cytotoxic ITGAE/CD103+ CD8+ TRM cells. Indeed, total CD8+ T-cell content is not associated with prognosis in ILC [56], although usually described as a key contributor of anti-tumor immunity [86]. We then further characterized CD8+ T lymphocyte subpopulations at the single-cell level with respect to their interactions with ILC cancer cells. Comparative analysis of ductal and lobular breast cancer highlights an enrichment in CD8+ T precursors, in particular CD8-KLF2 T cells, and a depletion in CD8-GZMH/TRM T cells (ITGAE/CD103+) in ILCs compared to IC-NSTs. CD8+ TRMs constitute a cytotoxic population with strong antitumor activity, expressing the heterologous E-cadherin receptor ITGAE/ITGB7, which is known to be involved in immunological synapse formation and function [58]. In addition, the TRM phenotype is negatively regulated by KLF2 [64], consistent with the accumulation of CD8-KLF2 T precursors we detected in ILC. Interestingly, we found a link between ITGAE and E-cadherin in ILC, suggesting that the E-cadherin/*CDH1* loss in ILC cancer cells induces a defect in CD8 TRM retention in lobular tissues, as shown in other cancers [58, 63, 68]. In addition, we demonstrate in co-culture experiments that both E-cadherin expression in breast cancer cells and ITGAE expression in CD8+ T lymphocytes are required to induce cytotoxicity and IFNγ secretion. These results support the notion that loss of *CDH1* in ILC induces escape from anti-CD8 immunity through defective interaction with the ITGAE receptor, as suggested in [63]. Altogether, our histopathological, biological, and functional findings provide supportive evidence that genetic inactivation of *CDH1* contributes to immune escape in breast cancer.

Evidence of the poor prognosis effect of TILs observed in ILCs is also found in more general studies of luminal breast cancers [87, 88, 89, 90]. It has been suggested that TILs could promote resistance to hormone therapy in luminal breast cancer, leading to a worse prognosis [91, 92]. In addition, estrogen receptor expression can directly promote resistance to anti-tumor immunity by various mechanisms, including the induction of granzyme B inhibitors such as PI-9 and the modulation of antigen presentation processes [93, 94]. Our findings are of clinical importance, as we describe an additional and lobular-specific mechanism of escape from CD8+ T-cell immunity, which will need to be taken into consideration for future implementation of breast cancer therapy requiring functional CD8-mediated cellular immunity. In particular, it is possible that the lack of interaction and cytotoxicity of CD8+ TRMs could specifically impact the efficacy of immunotherapies in E-cadherin-altered tumors, since CD8+ TRMs act as a major determinant of anti-tumor immunity and response to immunotherapy [55, 59, 60, 61, 62, 63]. The limitation of CAF

differentiation induced by E-cadherin/*CDH1* alteration may also influence the response to immunotherapy, as myCAF have been shown to be associated with immunosuppression and resistance to this treatment [11, 24, 25, 26, 27, 28, 29, 30].

Our work provides a detailed characterization of tumor microenvironment (TME) heterogeneity by defining four TEDI TME classes in ILC based on cellular composition, histological features, and prognostic outcomes. This classification may help identify patients likely to benefit from immunotherapy and/or TME-targeted treatments, alone or in combination with other therapies (e.g., hormone therapy) (Fig. 6B). TME class 1 ILCs (**T**GFβ/Wound-myCAF enriched) are associated with good prognosis and may be eligible for therapeutic de-escalation. TME class 2 ILCs (**E**CM/IFNαβ-myCAF enriched) are characterized by a high level of TREM2+/SPP1+ TAMs and are associated with poor prognosis, consistent with the adverse prognostic impact of M2-macrophages in ILC described in [56]. Anti-TREM2/SPP1 TAM therapy could represent a promising therapeutic target for TME class 2 ILCs. TME class 3 ILCs (Detox-iCAF enriched) show a high content of NKG2A+ NK cells, which could be targeted for anti-tumor effects [95], as well as endothelial cells, suggesting possible efficacy of anti-angiogenic therapy, in particular in combination with hormone therapy [96, 97]. Finally, TME class 4 ILCs (**I**mmune-cell enriched) could benefit from anti-inflammatory treatments to overcome endocrine resistance [91, 92] and could also be considered for immunotherapy strategies targeting non-CD8+ T cells to bypass CD8-related immune escape mechanisms. It is worth noting that a subset of ILCs may still respond to conventional immunotherapy, as suggested by the GELATO trial [98]. It remains to be determined whether these responsive tumors correspond to TME class 4, given their TIL enrichment, the low levels of immunosuppressive myCAF [27], and the remaining E-cadherin expression in a subset of this class.

In conclusion, we have shown that E-cadherin loss is at the root of key stromal features observed in ILC. In particular, we uncovered a mechanism connecting E-cadherin to the iCAF-to-myCAF transition, likely involving a heterologous interaction with ITGB1. Furthermore, TIL penetration into the tumor, favored by the accumulation of iCAF, is linked to immune escape mediated by a defective E-cadherin/ITGAE interaction compromising CD8+ T-cell retention and activation. Our data are important to consider for the development of future therapeutic strategies targeting the stroma in ILC and more broadly in cancer, as the mechanisms we describe (especially related to CAF differentiation) could be leveraged in different tumor types.

METHODS

This study was approved by the Institutional Review Board and Ethics committee of Institut Curie (DATA210135) and was conducted in accordance with all relevant ethical regulations.

Patients and samples

The study is based on a retrospective series of 251 patients who underwent surgery at Institut Curie between 2005 and 2008 for a primary ILC (prior to any therapy) and had frozen tumor tissues available for RNA sequencing. As we study breast cancer, only females were included throughout our study. This series was part of a larger cohort and has previously been published [10, 99, 100]. As previously reported, experienced breast pathologists (JCT, LD, and AVS) performed histopathological reviews of the patients in line with current standards [1]. In addition to the usual evaluation of overall stromal TILs [101], we also evaluated TILs specifically at the tumor center or invasive margin. As recommended in [102], the invasive margin was defined as the region centered on the border separating the host tissue from the malignant nests, with an extent of 1mm; central tumor corresponds to all the tissue inside the invasive margin. ILCs with non-null TIL content were further divided according to TIL spatial organization pattern: cases with a microscopically obvious difference (≥3%) between TILs at the invasive margin and at the tumor center were classified as "margin-predominant TILs", otherwise as "infiltrating TILs". Detailed characteristics of the retrospective ILC series are listed in the supplementary Table 4. Patients' survival data were also obtained, with a median follow-up of 9.5 years (range: 0.3-15.0 years). We also built tissue microarrays (TMAs) for 158 ER+ tumors from the retrospective ILC series, which we compared with 77 primary ER+ IC-NSTs (characteristics of the IHC retrospective series are detailed in Supplementary Table 1). In addition, we have established a prospective series of fresh samples from 6 ER+ ILC patients treated with surgery as the first step of treatment, for single cell analyses (characteristics of the prospective ILC cohort are detailed in Supplementary Table 3). As ILCs are more enriched in ER+ status, all comparisons between ILCs and IC-NSTs (using IHC, RNA-seq and scRNA-seq data) were performed on ER status matched cases, and ER+ cases were analyzed in both ILCs and IC-NSTs. Informed patient permission was obtained for the use of tissue samples for scientific purposes. Analysis of tumor samples was performed in accordance with the relevant national law and with recognized ethical guidelines (Declaration of Helsinki) on the protection of people taking part in biomedical research. Human experimental procedures for analyses of tumor microenvironment by F. Mechta-Grigoriou's lab were approved by the Institutional Review Board and Ethics committee of the Institut Curie Hospital group (approval

February 12, 2014) and CNIL (Commission Nationale de l'informatique et des Libertés approval no.: 1674356 delivered March 30, 2013). The Biological Resource Centre (BRC) is part of the Pathology Department in the Diagnostic and Theragnostic Medicine Department headed by Dr. A. Vincent-Salomon. BRC is authorized to store and manage human biological samples according to French legislation. The BRC has declared defined sample collections that are continuously incremented as and when patient consent forms are obtained (declaration number: DC-2008-57). The BRC has also been accredited with the AFNOR ISO20387 quality.

Immunostaining

All invasive breast carcinomas in this study underwent immunohistochemical evaluation as recommended by current guidelines [103, 104, 105] with antibodies directed against ER (clone 6F11, pH6, 20', 1:200, Leica #NCL-ER-6F11/2, RRID:AB_876939), progesterone receptor (PR) (clone 1A6, pH6, 20', 1:100, Leica #NCL-L-PGR, RRID:AB_563968) and HER2 (clone CB11, ph6, 15', 1:100, Leica #NCL-L-CB11, RRID:AB_563765). E-cadherin immunohistochemistry (pH9, 30', 1:100, clone 4A2C7, Invitrogen #180223, RRID:AB_2925243) was performed on all ILC. CAF and immune markers IHC have been performed on TMA with antibodies directed against SMA (pH6, 15', 1:200, clone 1A4, DAKO #IS611, RRID:AB_2891043), FAP (pH9, 60', 1:500, clone EPR20021, Abcam #ab207178, RRID:AB_2864720), ANTXR1 (pH9, 90', 1:50, clone EPNCI-R173-37, Abcam #241067), SDC1 (pH6, 30', 1:100, clone MI15, DAKO #M7228), MCAM (pH9, 30', 1:250, clone EPR3208, Abcam #ab75769 , RRID:AB_2143375), CD8 (pH9, 30', 1:100, clone 4B11, Novocastra #NCL-L-CD8-4B11, RRID:AB_442068), and CD103 (pH9, 30', 1:1000, clone EPR4166[2], Abcam #ab129202 , RRID:AB_11142856).

The staining process was performed on Leica BOND RX stainer as follow: 3-micrometer-thick formalin-fixed paraffin embedded sections were mounted on slides and labelled with antibody after a step of heat-mediated antigen retrieval using BOND Epitope Retrieval Solution 1 (pH6) (Leica, #AR9961) or 2 (pH9) (Leica, #AR9640) and blocking with Normal Horse Serum Blocking Solution (1:200, Vector #S2000-20). Antibody detection and hematoxylin counterstaining were done with BOND Polymer Refine Detection kit (Leica, #DS9800).

With respect to hormone receptor assessment, a threshold of 10% for ER/PR positivity was applied according to the *Groupe d'étude des facteurs pronostiques immunohistochimiques dans le cancer du sein* (GEFPICS) guidelines [106, 107]. Assessment of HER2 status was performed following ASCO/CAP recommendations [103]. Histomolecular subtypes were defined as follow: Luminal: ER ≥10% and HER2-negative; HER2: HER2-positive; triple-negative: ER-negative (<10%), PR-negative (<10%), and HER2 not amplified.

CAF markers were evaluated by histological score (H-score; 0 to 300), which corresponds to the sum of intensities (1 to 3) multiplied by the percentage of stained cells (0 to 100) for each intensity. The percentage of stained cells was defined as the ratio of labeled fibroblast surface area to stromal surface area. In order to have a precise estimation of FAP+ CAF clusters, we performed an analysis combining H-score results for several single IHC markers. We first excluded cases without significant FAP expression (H-score ≤1st quartile), to eliminate FAP+ CAF devoid cases. The FAP+ iCAF enriched cases were then defined as tumors with low ANTXR1 H-score, the ECM-myCAF enriched as cases with ANTXR1-High/SDC1-high H-scores and the other myCAF enriched as cases with ANTXR1-high/SDC1-low H-scores, on the basis of previous publications [11, 12, 23, 27, 31]. Gaussian mixture models were used to determine the thresholds between low and high H-scores for these FAP+ CAF cluster markers.

Immune markers (CD8, CD103) were analyzed using QuPath software v0.4.3 [108] (RRID:SCR_018257). QuPath's *positive cell detection* function was used to quantify the number of positive cells per mm². Parameter setting (including positivity thresholds), as well as control of all TMA analysis results, was carried out under the supervision of a pathologist, in order to minimize false positive and false negative rates.

Bulk RNA sequencing analyses

Bulk RNA sequencing analyses were performed using a protocol adapted from our previous work [33], with modifications specific to the present study. In brief, total RNA from tumors was extracted and subjected to *deoxyribonuclease* treatment (Nucleospin miRNA *deoxyribonuclease*, Macherey-Nagel, Düren, Germany). Overall, 500ng of good quality RNA with a majority of samples showing RIN >7 (BioAnalyzer, Agilent, Santa Clara, California, USA) were employed for Illumina library preparation using the Illumina® (San Diego, California, USA) TruSeq Stranded Total RNA Prep kit, which allows accounting for strand information. In a first step of ribodepletion, the RiboZero Gold kit was applied to eliminate both cytoplasmic and mitochondrial ribosomal RNAs. After fragmentation, cDNA synthesis was carried out, with the resulting fragments used for dA-tailing. This was followed by ligating TruSeq dual-index adapters. PCR amplification was then performed with 13 cycles able to generate the final barcoded cDNA libraries. Libraries were pooled equimolarly and subjected to quantitative PCR using the KAPA library quantification kit (Roche, Basel, Switzerland). Sequencing was carried out on the NovaSeq 6000 instrument from Illumina using a 2 x 100 cycle mode (paired-end reads, 2 x 100 bases) to obtain around 100 million clusters (200 million raw paired-end reads) per sample. Fastq files were generated from raw sequencing data after demultiplexing based on barcode sequences using bcl2fastq

(RRID:SCR_015058). Expression quantification was performed with SALMON (v0.13.1) (RRID:SCR_017036) using Ensembl96 (hg19), and the count matrix was normalized to TPM with tximport (R package).

ILC scRNA-seq and building a breast cancer cellular Atlas

Isolation of CAF, cancer cells and immune cells from ILC:

CAF, cancer cells and immune cells were isolated from 6 primary ER+ ILC samples obtained from patients treated at Institut Curie with upfront surgery (prior to any treatment) (see Supplementary Table 3 for further information on the ILC prospective cohort). Fresh tumor samples were collected shortly after surgery and underwent a digestion process before FACS cell sorting. Samples were cut into small fragments and digested for 45 minutes at 37°C with shaking (180 rpm) in CO2-independent medium (Gibco #18045-054) supplemented with 2 mg/ml of collagenase I (Sigma #C0130), 2 mg/ml of hyaluronidase (Sigma #H3506) and 25 mg/ml of DNase I (Roche #11284932001). The cells were then filtered through a 40µm cell strainer (Thermo Fisher Scientific #223635447) and resuspended in PBS+ solution (PBS, Gibco #14190; EDTA 2 mmol/L, Gibco #15575; Human Serum 1%, BioWest #S4190- 100) at a final concentration of 5.10^5 to 10^6 cells in 50 µL. For flow cytometry cell sorting, cells in suspension were stained for 30 minutes at room temperature with an antibody mix containing anti-EPCAM-BV605 (BioLegend, #324224, RRID:AB_2562518), anti-CD31-PECy7 (BioLegend, #303118, RRID:AB_2247932), anti-CD45-APCCy7 (BD Biosciences, #BD-557833, RRID:AB_396891), anti-CD235a-PerCP/Cy5.5 (BioLegend, #349109, RRID:AB_2562705), anti-CD29-Alexa Fluor 700 (BioLegend, #303020, RRID:AB_2130078) and anti-FAP-APC (primary antibody, R&D Systems, #MAB3715 , RRID:AB_2102368). DAPI (2.5 µg/mL; Thermo Fisher Scientific, #D1306, RRID:AB_2629482) was added just before flow cytometry sorting on the BDFACS ARIA III sorter (BD Biosciences). For each antibody, compensations were done using a single staining on anti-mouse IgG and negative control beads (BD Biosciences, #552843). FlowJo version 10.8.1 was used to analyze the data. Cells were first gated based on forward (FSC-A) and side (SSC-A) scattering to remove debris, and DAPI positive dead cells were excluded. Single cells were then selected based on SSC-A versus SSC-W parameters. Cell sorting was then carried out to recover separately immune cells (CD45+), epithelial cells (EPCAM+) and CAF (EPCAM-, CD45-, CD31-, CD235a-).

Single-cell RNA-seq analysis of ILC:

Upon isolation, CAF, CD45+ immune cells and EPCAM+ cells were directly collected (at a concentration of 200,000 cells/mL) into RNase-free tubes (Thermo Fisher Scientific, #AM12450)

precoated with DMEM (GE Life Sciences, #SH30243.01) supplemented with 10% FBS (Biosera, #1003/500). The Chromium system from 10X Genomics was used for single-cell capture, lysis, and cDNA library creation, with the following kits: Chromium Next GEM Single Cell 3' GEM, Library & Gel Bead Kit v3.1 (10X Genomics, #1000141) and Chromium Next GEM Chip G Single Cell Kit (10X Genomics, #1000136). The manufacturer's instructions were followed for the generation of gel beads in emulsion (GEM), barcoding, post GEM-reverse transcription cleanup, and cDNA amplification. Targeted cell recovery was 5,000 cells per sample. Cells were placed onto the Chromium Single cell G chips as recommended, and 12 cycles of cDNA amplification were done. The quality and quantity of cDNA were determined using an Agilent 2100 Bioanalyzer and the Agilent High Sensitivity DNA Kit (Agilent, #5067-4626). The library was constructed in accordance with the 10X Genomics procedure. Libraries were then sequenced on the Illumina NovaSeq platforms at a depth of 50,000 reads per cell. The raw data were processed using the 10X Cell Ranger pipeline version 6.0.0, which included demultiplexing raw base call (BCL) files into FASTQ files, alignment, filtering, barcode, and Unique Molecular Identifiers (UMI) counting. The reads were aligned to the GRCh38 human genome assembly.

Quality Control: Based on the distribution of the unique genes found (nonzero count) in each cell for each sample, we first filtered out low-quality cells, empty droplets, and multiplet captures. Cells with fewer than 1,200 genes and those with more than 6,000 genes were removed (more than 4,000 genes for immune cells). To exclude dying cells or low-quality cells with substantial mitochondrial contamination, cells with a fraction of mitochondrial genes more than 10% were eliminated. Following these quality-control criteria, 36,090 cells (patient 1 = 4,689 cells; patient 2 = 7,697 cells; patient 3 = 5,026 cells; patient 4 = 3,244 cells; patient 5 = 4,889 cells; patient 6 = 10,545 cells), including 22,830 immune cells, 6,378 CAF and 6,865 EPCAM+ cells were retained for downstream analyses.

Normalization, Data Integration and data visualisation: Integration of the 6 ILC scRNA-seq was done after library-size normalization of each cell (NormalizeData function with default parameters), using Seurat functions FindIntegrationAnchors (dimensional reduction done with Reciprocal PCA) and IntegrateData (with thirty principal components used in the weighting procedure). Identification of features that were outliers on a mean variability plot was performed using FindVariableFeatures, with *vst* selection method and 2000 features selected as top variable features. Data were scaled using the ScaleData function based on variable features. Principal component analysis (PCA) dimensionality reduction was run using default parameters. Thirty

principal components (PCs) were retained for data integration based on the Elbow Plot, which indicated a plateau at this level. This choice is also in line with common practice in scRNA-seq analyses using Seurat. For visualization of the data, the nonlinear dimensional reduction technique UMAP was applied using the RunUMAP function from Seurat.

Clustering and annotation:

CAF, immune cells and epithelial cells were clustered and annotated separately after isolation of the three populations based on clustering and cell marker expression (VIM/DCN, PTPRC and EPCAM, respectively). A graph-based clustering approach was used to cluster the cells using FindNeighbours and FindClusters functions (resolution and optimal number of clusters were defined using the silhouette and clustering tree method (clustree R package v0.4.4)). Cell type clusters were annotated by using the label transfer approach implemented in Seurat, applying the *FindTransferAnchors* and *TransferData functions* (using [57] for T cells and [27] for FAP+ CAF as reference), canonical markers (EPCAM: epithelial cells, PTPRC: immune cells, ERG: endothelial cells, LYVE-1: lymphatic endothelial cells, DCN: fibroblasts, PI16: universal fibroblasts, ANTXR1: myCAF-S1 / FAP+ myCAF, CXCL12: iCAF-S1 / FAP+ iCAF, SDC1: ECM-myCAF, LAMP5: TGFβ-myCAF, PTGER3: Wound-myCAF, GPC3: Detox-iCAF, DLK1: IL-iCAF, CD74: IFNγ-myCAF, MCAM: CAF-S4 / CAP, FABP4: adipocytes, TP63: myoepithelial cells, CD3E: T cells, CD8A: CD8+ T cells, CD4: CD4+ T cells, FOXP3: regulatory T cells, TNFRSF18: follicular helper T cells, NCAM1: NK cells, FCGR3A: NK-CD16 cells, KLRC1: NK-NKG2A cells, MS4A1: B cells, MZB1: plasma cells, IL3RA: pDC, CLEC9A: cDC1, CD1C: DC2/Mo-DC, FCER1A: Mono-DC, LAMP3: LAMP3+ DC, CD14: monocytes/macrophages, APOE: macrophages, FOLR2: FOLR2+ TAM, SPP1: SPP1+ TAM, TREM2: TREM2+ TAM, FUT4: neutrophils, TPSA1B: mast cells), and gene signatures (Supplementary Data 1). In addition, CNV profiles were generated, notably to help distinguish normal from tumoral epithelial cell types, using InferCNV (R package version 1.14.0). Fibroblasts were used as reference and epithelial cells as query. The analysis was run using cluster_by_groups set to TRUE, analysis_mode set to subclusters, otherwise default parameters were used. Overall, 47 cell types and states were identified in the ILC single-cell dataset.

Building a reference lobular and ductal single-cell RNA-seq atlas

In order to make comparisons between IC-NST and ILC cell populations, as well as to deconvolute transcriptomic data from large series of ductal and lobular tumors, we established a lobular and ductal single-cell RNA-seq atlas. To do this, we integrated our 6 ER+ ILCs scRNA-seq data into a single-cell breast cancer atlas from public datasets [41, 50, 51] established in [33]. All patients included

in the atlas are treatment-naïve (samples obtained from biopsy or surgery performed before any (other) local or systemic therapy). This ILC & IC-NST scRNA-seq atlas comprises 35,995 cells from ILC, 29,426 cells from ER+ IC-NST, 30,926 cells from triple negative breast cancers, 3,909 cells from HER2+ breast cancers, and 8,881 normal fibroblasts from mammoplasty. The overall resolution, as assessed by the number of detected genes per cell, is comparable between the two cohorts (median = 1,578 detected genes per cell in the IC-NST cohort *versus* 2,019 detected genes per cell in the ILC cohort). Integration was performed using the FASTMNN algorithm. All cell populations were re-annotated after a new clustering step performed on the ILC & IC-NST atlas, with the exception of fibroblastic populations for which the previous annotation was retained. Cluster annotation was carried out on the basis of previously performed annotation (see previous section for ILC and [33] for IC-NST annotation), label transfer (from [57] for T cells), canonical markers (EPCAM - epithelial cells, PTPRC - immune cells, ERG - endothelial cells, LYVE-1 - lymphatic endothelial cells, DCN - fibroblasts, PI16 - universal fibroblasts, ANTXR1 - FAP+ myCAF, CXCL12 - iCAF-S1 / FAP+ iCAF, SDC1 - ECM-myCAF, LAMP5 - TGFβ-myCAF, PTGER3 - wound-myCAF, GPC3 - detox-iCAF, DLK1 - IL-iCAF, CD74 - IFNγ-myCAF, MCAM - CAF-S4, FABP4 - adipocytes, TP63 - myoepithelial cells, CD3E - T cells, CD8A - CD8 T cells, CD4 - CD4 T cells, FOXP3 - regulatory T cells, TNFRSF18 – follicular helper T cells, NCAM1 - NK cells, FCGR3A - NK-CD16 cells, KLRC1 - NK-NKG2A cells, MS4A1 - B cells, MZB1 - plasma cells, IL3RA - pDC, CLEC9A - cDC1, CD1C – DC2/Mo-DC, FCER1A – Mono-DC, LAMP3 - LAMP3+ DC, CD14 - monocytes/macrophages, APOE - macrophages, FOLR2 - FOLR2+ TAM, SPP1 - SPP1+ TAM, TREM2 - TREM2+ TAM, FUT4 – neutrophils, TPSA1B - mast cells), and signatures (Supplementary Data 1). Confusion matrices (using pheatmap R package (RRID:SCR_016418)) were carried out to check the consistency of the new annotations with the previous ones. The atlas was composed of 47 clusters, including ILC cancer cells, IC-NST cancer cells, normal epithelial cells, myoepithelial cells, four endothelial cell clusters (adipo-EC, angio-EC, ap-EC, lymphatic-EC), seven FAP+ CAF / CAF-S1 clusters (Detox-iCAF, IL-iCAF, IFNγ-iCAF, ECM-myCAF, TGFβ-myCAF, Wound-myCAF, IFNαβ-myCAF), three CAP/CAF-S4 clusters (ECM-CAP, Contractile-CAP, Ag-CAP), normal fibroblasts, universal fibroblasts, two B cell clusters (B naïve cells, B memory cells), plasma cells, five CD4+ T cell clusters (CD4 naïve T cells, CD4-IL7R memory T cells, CD4-CD69 activated memory T cells, CD4 TFH cells, CD4 T regulatory cells), five CD8+ T cell clusters (CD8-KLF2, CD8-GZMK and CD8-XCL1 precursors T cells, CD8-GZMH transitional T cells, CD8-FCGR3A T cells), two NK cell clusters (NK-CD16 and NK-NKG2A cells), innate lymphoid cells (ILC3), two monocyte clusters (CD14+ monocytes, CD16+ monocytes), four

macrophage clusters (CXCL10+ macrophages, FOLR2+ TAM, TREM2+ TAM, SPP1+ TAM), four dendritic cell clusters (LAMP3+ DC, Mo-DC, cDC1, pDC), and mast cells.

Ligand-Receptor analysis of scRNA-seq data

Ligand-receptor analyses were carried out with the R package CellChat version 1.5.0 (RRID:SCR_021946) on the basis of an updated CellChatDB database. The E-cadherin pathway has been enriched by the CDH1-ITGB1 interaction [73, 74]. Overexpressed genes and interactions were computed with identifyOverExpressedGenes and identifyOverExpressedInteractions respectively, with default parameters. Communication probabilities were computed using computeCommunProb with a more stringent truncated mean (35%) than the default method 'trimean' (25%) leading to the detection of a smaller but more relevant number of interactions. FilterCommunication was used to filter cell-cell communications, and computeCommunProbPathway with default settings was used to compute the communication pathway probability.

Deconvolution of bulk RNA-seq data

Using the BayesPrism algorithm version v2.0 [109], bulk RNA-seq data of 251 ILCs from our retrospective cohort, 446 early ER+ IC-NSTs from the TCGA cohort [110] and 78 TN IC-NSTs from Institut Curie SCANDARE cohort [52] were deconvolved. As input for previous information, a raw count matrix of 109,137 cells after quality control from our ILC & IC-NST scRNA-seq atlas has been used. Labels were obtained from the above-mentioned annotation of 47 cell types and states. Mitochondrial and ribosomal protein coding genes were removed since they are highly expressed and do not help discriminate across cell types. Following the BayesPrism's authors' recommendation, MALAT1 and genes from chrX and chrY were also removed. We exclusively deconvolved protein-coding genes to decrease batch effects and speed up calculation. Default parameters to control Gibbs sampling and optimization were used. The final cell type fraction estimation in each bulk RNA-seq sample was obtained using the updated theta matrix and was used for downstream analysis.

Spatial transcriptomics

Spatial transcriptomics was performed following a procedure adapted from our previously published work [33], with details and study-specific modifications described below.

Sample preparation: Four frozen BC samples were selected based on tissue architecture, TIL spatial organization, and RNA quality (RIN > 8). The "Visium Spatial Tissue Optimization Slide

and Reagent Kit" (10X Genomics;#PN-1000193) was used to optimize permeabilization conditions for BC tissues. Briefly, sections were fixed, stained and permeabilized at different time points to capture mRNA, followed by reverse transcription to generate fluorescently labeled cDNA. The permeabilization time yielding the highest fluorescence signal with the lowest background diffusion was selected. Cryostat sections of 10 µm thickness were placed on Visium Spatial Gene Expression slides (10X Genomics, PN-1000184). Slides were incubated for 1 min at 37 °C, fixed in methanol for 30 min at −20 °C, stained with Hematoxylin and Eosin (H&E), and imaged at high resolution. After imaging, the coverslip was removed by immersion in water, and the slide was mounted in a plastic slide cassette. Spatial gene expression processing, including tissue permeabilization, second-strand synthesis, and cDNA amplification, was then performed according to the manufacturer's instructions (10X Genomics; #CG000239), following the workflow previously reported in [33]. cDNA quality was subsequently assessed using the Agilent High Sensitivity DNA Kit (Agilent, #5067-4626). Spatial gene libraries were generated using the Visium Spatial Library Construction Kit (10X Genomics, PN-1000184).

Processing of the data and deconvolution: Spatial transcriptomic data were processed using SpaceRanger software v1.2.2 (10x Genomics). Raw base call (BCL) files were demultiplexed and aligned to the GRCh38 reference genome. Alignment of barcoded spot patterns and selection of tissue-covered spots were performed using Loupe Browser (10x Genomics). The resulting count matrices were analyzed in Seurat v5.3.1 for log2 normalization, scaling, and dimensionality reduction. Spatial deconvolution was performed in Python3 using cell2location version 0.1. The BC atlas described above was used to estimate reference cell type signatures with RegressionModel, with categorical_covariate_keys set to patient ID,and all other parameters left at default values. Normal and universal fibroblasts were excluded from the reference used for deconvolution. A total of 43 distinct cell types and states were retained. Each Visium section was analyzed independently. Based on manual examination of the slides, N_cells_per_location was set to 15 and detection_alpha to 20. The number of epoch was set to 20,000. For downstream visualization and analysis, the q05_cell_abundance_w_sf matrix generated by cell2location was discretized by rounding values up for non-malignant cell types and down for cancer cells, according to microscopically identifiable cell types and observed cell densities as assessed by a pathologist.

Mouse models of ILC

All animal experiments were approved by the Dutch Animal Ethical Committee and conducted in compliance with the Netherlands Cancer Institute and Dutch Animal Welfare guidelines. Generation of *WapCre;Cdh1$^{F/F}$;Pten$^{F/F}$* (WEPtn) and *WapCre;Pten$^{F/F}$* (WPtn) mice has been described previously [111]. *WapCre;Cdh1$^{F/F}$;Col1a1$^{invCAG\text{-}Pik3cE545KR\text{-}IRES\text{-}Luc}$* (WEE545K) mice were generated by cloning human *Pik3ca* bearing the constitutively activating mutation E545K in the *Frt-invCag-IRES-Luc* shuttle vector using FseI and PmeI, resulting in *Frt-invCag-Pik3ca^{E545K}-IRES-Luc*. Flp-mediated knockin of the shuttle vector in *WapCre;Cdh1$^{F/F}$* GEMM-ESCs was performed as described previously [112]. Chimeric animals were crossed with *WapCre;Cdh1$^{F/F}$* mice or wildtype FVB/n mice to generate the experimental animal cohorts proficient (WE545K) or deficient (WEE545K) in *Cdh1*. All breast cancer GEMMs are FVB/n background. All mice were housed on standard 12 hr day/night cycle, in individually ventilated cages with ad libitum food. Room temperature was 21°C with a humidity of 55%.

Transcriptomics of mouse tumors

Tumors were harvested from the described models (n=3 mice per model) at ages that yielded comparable tumor sizes between the E-cadherin-proficient and -deficient setting. This means that WEPtn- and WEE545K- derived tumors were harvested at 20 weeks of age and WPtn- and WE545K-derived tumors were harvested at 40 weeks of age. All animal experiments were conducted with female mice. Maximum permitted cumulative tumor volume of 2000 mm3 was not reached in any of the experiments. Tumor volume was calculated as: 0.5 x (length x width^2). All animals were euthanized using CO_2. Samples were processed and sequenced as described previously [113].

Deconvolution of mouse transcriptomics using scRNAseq reference

CIBERSORTx [114] docker version was utilized to estimate cell-type proportions from bulk transcriptomics samples harvested from indicated mouse models. The signature matrix needed for deconvolution was created using previously generated scRNAseq data containing four ILC mouse models [113 115]. In accordance with CIBERSORTx [114] documentation, both the signature matrix and bulk RNA samples were TPM normalized and deconvoluted with Smode and -fraction threshold 0 as recommended when the signature matrix is made using droplet methods like 10x chromium. The resulting CIBERSORTx output was moved to R version 4.2.3 and visualized with R package ggplot2 version 3.4.4 where necessary values needed for the addition of error bars (mean +/- SEM) were calculated using summarySE from R package Rmisc version 1.5.1.

Isolation and characterization of primary FAP+ CAF / CAF-S1 clusters for functional assays

Fresh ER+ ductal breast cancer samples received after surgery were cut into fragments of approximately 1 mm^3, put either in plastic petri dishes or in petri dishes coated with type I collagen at a final concentration of 9 µg/ml (Institut De Biotechnologie Jacques Boy, #207050357) and cultured in DMEM (Gibco, #41966-029) supplemented with 10% heat inactivated FBS (Biosera, #FB-1003-500) and 1% streptomycin and penicillin (Sigma, #p4333) for 2-3 weeks at 37°C. Media was renewed every 3 days for 2-3 weeks. When fibroblasts reached at least 50% confluency, they were detached using TrypLE (Gibco, #12605-010), centrifuged at 1200 rpm (129 x g) for 5 min and plated in new plastic plates or collagen-coated plates using DMEM supplemented as above. All experiments using CAF primary cell lines were not performed beyond passage 10 to avoid fibroblast senescence. Verification of the identity of FAP+ CAF cluster cells was determined by flow cytometry. These fibroblasts were detached and 5 x 10^4 cells were then stained for 20 min at RT with an antibody mix containing anti-CD29-Alexa Fluor 700 (1:100, BioLegend, #303020, RRID:AB_2130078), anti-FAP-APC (1:100, R&D Systems, #MAB3715, RRID:AB_2102368), anti-ANTXR1-Alexa Fluor 405 (1:25, Novus Bio, #NB100-56585AF405, RRID:AB_3160883), anti-SDC1-BUV737 (1:25, BD Biosciences, #612834, RRID:AB_2870156), anti-LAMP5-PE (1:10, Miltenyi Biotec, #130-109-156, RRID:AB_2652589), anti-GPC3-Alexa Fluor 594 (R&D systems, 1:20, #FAB2119T , RRID:AB_3647838), anti-DLK1-Alexa Fluor 488 (R&D systems, 1:20, #FAB1144G , RRID:AB_3645938), anti-CD9-BV711 (BD Biosciences,1:100, #743050, RRID:AB_2741246) and anti-CD74-BV786 (BD Biosciences, 1:100, #743736, RRID:AB_2741709). All antibodies except FAP were purchased already conjugated with fluorescent dyes. Anti-FAP primary antibody was conjugated with fluorescent dye Zenon APC Mouse IgG1 labeling kit (1:100, Thermo Fisher Scientific, #Z25051, RRID:AB_2736969). Isotype control antibodies for each CAF marker used were: iso-anti-CD29-Alexa Fluor 700 (Alexa Fluor 700 Mouse IgG1 κ Isotype Ctrl Antibody, 1:100, BioLegend, #400144, RRID:AB_2923250), iso-anti-FAP-APC (Mouse IgG1 κ Isotype Control, R&D Systems, 1:200 , #MAB002, RRID:AB_357344), iso-anti-ANTXR1-Alexa Fluor 405 (Mouse IgG1 Alexa Fluor 405-conjugated Antibody, 1:100, R&D systems, #IC002V, RRID:AB_3654370), iso-anti-SDC1-BUV737 (BUV737 Mouse IgG1 κ Isotype Control; 1:100, BD Biosciences, #612758, RRID:AB_2870089), iso-anti-LAMP5-PE (PE human IgG1 REA Control Antibody, 1:10, Miltenyi Biotec #130-104-613, RRID:AB_2661678), iso-anti-GPC3-Alexa Fluor 549 (Mouse IgG2A Alexa Fluor594-conjugated Isotype Control, 1:20, R&D systems, #IC003T, RRID:AB_3654373), iso-anti-DLK1-Alexa Fluor 488 (Mouse IgG2B Alexa Fluor488-conjugated Isotype Control, 1:20, R&D systems, IC0041G, RRID:AB_10718124), iso-anti-CD9-BV711 (BV711 Mouse IgG1 κ Isotype Control, 1:100, BD

Biosciences, #563044, RRID:AB_2869449) and iso-anti-CD74-BV786 (BV786 Mouse IgG1 κ Isotype Control, 1:100, BD Biosciences, #563330, RRID:AB_2869484). Cells were then washed and acquired on the BD LSRFortessa™ analyzer (BD biosciences).

For all flow cytometry analysis, at least 5 × 10^5 events were recorded for each sample. Compensations were performed using single staining of anti-Mouse IgG and Negative control particle set (BD biosciences, #552843) with each antibody. Data analysis was performed using FlowJo version X 10.0.7r2. Cells were first gated based on their size and granularity. Viable cells were identified by excluding LIVE/DEAD positive cells.

Silencing experiment using small-interference RNA (siRNAs)

For the short interfering RNA (siRNA) experiment, 2,5x10^5 FAP+ CAF primary fibroblasts or MCF7/T47D breast cancer cells were plated in a 6-well plate and transfected with 10 nM of siRNA the same day before adherence. Transfected cells were incubated in DMEM supplemented with 10% heat inactivated FBS for 72 h at 37°C and 1.5% O2. The siRNA control used was ON-TARGETplus Non-targeting siRNA (Target sequence UGG-UUU-ACA-UGU-UGU-GUG-A, Dharmacon #D-001810-02-05). ITGB1 silencing in primary fibroblasts was performed with two distinct siRNAs targeting ITGB1 (siITGB1#1: GUG-CAG-AGC-CUU-CAA-UAA-A and siITGB1#2: GGU-AGA-AAG-UCG-GGA-CAA-A, Horizon Discovery, #LQ-004506-00-0005). *CDH1* silencing in MCF7 (RRID:CVCL_0031) and T47D (RRID:CVCL_0553) breast cancer cells was achieved using two different siRNA targeting *CDH1* (siCDH1#1: GAG-AAC-GCA-UUG-CCA-CAU-A and siCDH1#2: GGG-ACA-ACG-UUU-AUU-ACU-A, Horizon Discovery, #LQ-003877-00-0005). Transfections were performed with DharmaFECT 2 Transfection Reagent (Horizon Discovery, #T-2005-01) according to manufacturer's instructions. Efficient *CDH1* and *ITGB1* silencing were validated after 72 h by western blot. Before use, cell lines were authenticated by STR profiling and routinely tested for absence of mycoplasma contamination using PCR-based assays.

Protein extraction and western blot

Protein extraction and western blot analyses were performed as previously described [33], except for the primary antibodies used in the present study.

Protein extraction: Cells were washed in cold PBS (Gibco #14190) and lysed in 100 µl of Laemmli buffer (BioRad, #1610737) supplemented with DTT to a final concentration of 50 mM (Thermoscientific, #11896744). Samples were heated at 95°C for 10 min, sonicated for 10 min using 30 s ON/30 s OFF cycles, and centrifuged for 10 min at 13.000g at 4°C. Protein extracts were stored at −80°C until use.

Western blot: 15 µl of proteins extracts were loaded onto NuPAGE Novex 4-12% Bis-Tris mini gels (Thermofischer, #NP0321BOX). Electrophoresis was performed for 2h at 120V in 1X NuPAGE® MOPS SDS Running Buffer (for Bis-Tris Gels only) (Invitrogen, #NP0001) in electrophoresis. Proteins were then transferred onto a 0.45 µm nitrocellulose membrane (GE Healthcare #10600002) and membranes were incubated overnight at 4°C with the following primary antibodies: E-cadherin monoclonal antibody (1:1,000, Invitrogen #MA5-12547, RRID:AB_10982676); Human Integrin B1 monoclonal antibody (1:1,000, abcam #ab3167, RRID:AB_303570) and Actin (1:10,000; Sigma #A5441, RRID:AB_476744). After washing, membranes were incubated for 1 h with the appropriate peroxidase-conjugated secondary antibodies (Jackson ImmunoResearch Laboratories #115-035-003, RRID:AB_10015289), and signal detection was performed using enhanced chemiluminescence (Western Lightning Plus-ECL, PerkinElmer #NEL103E001EA). Immunoblot quantification was carried out using ImageJ (RRID:SCR_003070).

Co-culture of FAP+ CAF (CAF-S1) clusters with MCF-7 and T47D cell lines

For co-culture assays, 7 x 10^4 FAP+ CAF cluster cells transfected or not for 72 hours with siRNA targeting *ITGB1* were co-cultured in the presence of 3.5 x 10^4 MCF-7 (RRID:CVCL_0031) or T47D (RRID:CVCL_0553) breast cancer cells transfected or not with siRNA targeting *CDH1* in 6-well plates at 37°C, 1.5% O2. Following 48 hours of co-culture, cells were collected, washed in PBS and stained for 20 min at RT with the same antibody mix as detailed above (#*Isolation and characterization of primary FAP+ CAF / CAF-S1 clusters for functional assays*). Total samples were acquired on the LSRFortessa™ analyzer (BD biosciences) and data were analyzed using FlowJo 10.5.2 software (RRID:SCR_008520).

Isolation of CD8+ ITGAE/CD103+ T lymphocytes

Primary immune cells were isolated from peripheral blood of healthy donors (informed consent) obtained from the “Etablissement Français du sang” through a convention with the Institut Curie, Paris, France. Briefly, peripheral blood mononuclear cells (PBMC) were isolated using Lymphoprep (STEMCELL #07861) and CD8+ T cells were selectively isolated by magnetic cell separation using a specific isolation kit (Human CD8+ T Cell Isolation Kit, STEMCELL #17953). To selectively isolate CD8+ ITGAE/CD103+ T cells, CD8+ T lymphocytes were stained for 20 min at RT with CD103 specific antibody (1:50, BD Biosciences, #350206, RRID:AB_10641843), followed by 20 min of incubation with PE microbeads (Miltenyi, #130-048-801, RRID:AB_244373) allowing a magnetic separation of this specific population.

For co-culture experiments, 5 x 10^4 MCF7 (RRID:CVCL_0031) or T47D (RRID:CVCL_0553) breast cancer cells transfected or not with siRNA targeting *CDH1* were plated on 24-well plates in DMEM supplemented with 10% heat-inactivated FBS and 1% Penicillin streptomycin at 1.5% O_2 overnight for complete adherence. The medium was then removed and 500 µl of DMEM supplemented with 1% FBS containing 5 x10^5 CD8+ T cells were added. Co-cultures were maintained for 24h at 37°C, 20% O_2.

After incubation, $CD8^+$ T lymphocytes were collected and analyzed by flow cytometry. Cells were first stained for 10 min at RT with a violet live/dead marker (1:1000 BD Bioscience #565388) to exclude dead cells. After washing with PBS+ solution, T lymphocytes were incubated during 15 min at RT with a pool of fluorescent-conjugated primary antibodies containing anti-CD45-BUV395 (1:100; BD Biosciences #557833, RRID:AB_396891), anti-CD3-AlexaFluor700 (1:50; BD Biosciences #557943, RRID:AB_396952), and anti-CD8-BV510 (1:50; BD Biosciences, #563919, RRID:AB_2722546). For intracellular staining of perforin, granzyme B, granzyme K and IFNγ, cells were fixed in 4% paraformaldehyde for 15 min at RT and then incubated with an antibody pool containing anti-Perforin-FITC (1:25; BD Biosciences #563764, RRID:AB_2738411), anti-Granzyme B-BV421 (1:25; Biolegend, #396415, RRID:AB_2924597), anti-granzyme K-FITC (1:25; Biolegend, #370508, RRID:AB_2632846) and anti-IFNγ BV786 (1:50; BD Biosciences, #563731, RRID:AB_2738391) or the corresponding mouse IgG2b-FITC isotype control (1:25; BD Biosciences, #556655, RRID:AB_396519), mouse IgG1-BV421 isotype control (1:25; biolegend, #400429, RRID:AB_10900998), Mouse IgG1-FITC isotype control (1:25; Biolegend, #400138, RRID:AB_493442), and BV786 mouse IgG1 isotype control (1:100; BD Biosciences, #563330, RRID:AB_2869484). Antibodies were resuspended in PBS+ solution with 0.2% saponin (Sigma-Aldrich #S7900). Cell analysis was performed on LSRFORTESSA (BD Biosciences). At least 1×10^5 events were recorded. Compensations were performed using single staining on anti-mouse IgG and negative control beads (BD Biosciences #552843) for mouse antibodies, on AbC Total compensation beads (Molecular Probes #A10513) for rat antibody and on ArC reactive beads (Molecular Probes #A10346) for Live/Dead staining (1:1000, Thermo Fisher, #L34955). Data analysis was performed using FlowJo version 10.4.2. Cells were first gated based on forward (FSC-A) and side (SSC-A) scatters. Dead cells were excluded based on their positive staining for live/dead marker. Cells were then gated on $CD45^+$, $CD3^+$, $CD8^+$ cells and next examined for expression of Granzyme B, Granzyme K, perforin and IFNγ.

Transwell Migration Assay

The transwell migration assay was adapted from our previously published protocol [33], with modifications in the migrating immune cell population, co-culture conditions, and incubation time. For migration assay, $5x10^4$ primary FAP+ CAF fibroblasts transfected or not with siRNA targeting *ITGB1* were seeded in the lower chamber of 24-well transwell inserts with 0.4 µm pores (Corning HTS Transwell 24 wells #CLS3413) in the presence or absence of MCF7 (RRID:CVCL_0031) or T47D (RRID:CVCL_0553) breast cancer cells transfected or not with siRNA targeting *CDH1* (siCDH1#1: GAG-AAC-GCA-UUG-CCA-CAU-A and siCDH1#2: GGG-ACA-ACG-UUU-AUU-ACU-A, Horizon Discovery, #LQ-003877-00-0005). Cells were maintained overnight in DMEM supplemented with 10% heat-inactivated FBS and 1% penicillin/streptomycin under 1.5% O2 to allow cell adherence. CD8+ T lymphocytes were then added to the upper chamber at $2,5x10^5$ cells in 50 µl DMEM containing 1% FBS and incubated for 24h at 37°C under 20% O_2. Cells recovered from the upper and lower chambers were collected separately. Before counting, 0.5 µl of 10 µm carboxylated beads (Polyscience #18133) and DAPI (3 µM) were added to each sample. Cell quantification was done by Flow Cytometry using precision beads for normalization. Migration was expressed as the percentage of cells detected in the lower chamber relative to the total number of recovered T lymphocytes.

Statistical analysis

GraphPad Prism software (version 9.5.1) (RRID:SCR_002798) or the R environment (https://cran.r-project.org, version 4.3.1) were used for all statistical analyses and data visualization. For qualitative data, baseline characteristics were reported as percentages and frequencies; for continuous variables, values were expressed as mean, standard deviation, and range. Fisher's exact test or Chi-squared test was used to assess associations between categorical variables. For the sake of readability, only populations with a proportion greater than 3% have been indicated in the barplots. Depending on the distribution of the continuous variables as assessed by the Shapiro-Wilk test, either the Wilcoxon rank sum test (Mann-Whitney) or Student's t-test was used. Overall survival (OS) was defined as the time from breast cancer diagnosis until the date of death. Breast cancer-specific survival (BCSS) was defined as the time from breast cancer diagnosis until the date of death from breast cancer. Patients still alive were censored at the date of last news. Distant metastasis-free interval (DMFI) was defined as the interval from breast cancer diagnosis until the first distant recurrence. Patients with no distant recurrence were censored at the date of last news. OS, BCSS, and DMFI were estimated using the Kaplan–Meier method, with comparisons between different subgroups made using log-rank testing. Univariate and multivariate Cox analyses were additionally employed to evaluate the

prognostic value of these subgroups. Variables that were significantly associated with survival in univariate analysis were included in the multivariate model. A p-value ≤0.05 was considered statistically significant. All statistical tests were two-sided unless otherwise indicated.

Data availability

Raw scRNA-seq data from 6 ILCs generated in this study, including all sorted cell populations, are available on European Genome-Phenome Archive platform (https://ega-archive.org) under the controlled accession number: EGAS50000000761. Raw and processed spatial transcriptomics data generated in this study are available on the European Genome-Phenome Archive (accession number: EGAS50000001735) and from the Figshare data repository link https://doi.org/10.6084/m9.figshare.31429790. The scRNAseq data for IC-NST were obtained from [33] based on public datasets [41] [https://singlecell.broadinstitute.org/single_cell/study/SCP1039]; [50] [https://ega-archive.org/datasets/EGAD00001006608]; [51] [https://www.ncbi.nlm.nih.gov/geo/query/acc.cgi?acc=GSE161529]. Raw and processed RNA-seq data from the Institut Curie ILC retrospective series are available on the European Genome-Phenome Archive (accession number: EGAS50000001760) and via Figshare (https://doi.org/10.6084/m9.figshare.28416968) for patients who provided consent for public data sharing. Raw and processed RNA-seq data from the TNBC SCANDARE Curie cohort are available on the European Genome-Phenome Archive (accession number EGAS50000000970) and in the Figshare data repository at https://doi.org/10.6084/m9.figshare.28485827. The controlled access is required as raw data contain identifying patient information. Data access can be granted via the EGA with completion of an institute data transfer agreement.

The raw sequence data from the mouse models have been previously published in [113] and are available in the Gene Expression Omnibus database under accession Number GSE214933 [https://www.ncbi.nlm.nih.gov/geo/query/acc.cgi?acc=GSE21493]. The remaining data are available within the Article and Supplementary Information. Source data are provided with this paper and are also available from the figshare hyperlink: https://doi.org/10.6084/m9.figshare.31438159.

Code availability

Codes used for this study are available on Figshare under the https://doi.org/10.6084/m9.figshare.31427711.

REFERENCES

1. Board WHOCoTE. *Breast tumours*, 5th edition edn. International Agency fo Research on Cancer (2019).

2. Berx G*, et al.* E-cadherin is a tumour/invasion suppressor gene mutated in human lobular breast cancers. *The EMBO journal* **14**, (1995).

3. Christgen M*, et al.* Lobular Breast Cancer: Histomorphology and Different Concepts of a Special Spectrum of Tumors. *Cancers* **13**, 3695 (2021).

4. Sastre-Garau X*, et al.* Infiltrating lobular carcinoma of the breast. Clinicopathologic analysis of 975 cases with reference to data on conservative therapy and metastatic patterns. *Cancer* **77**, 113-120 (1996).

5. Ferlicot S*, et al.* Wide metastatic spreading in infiltrating lobular carcinoma of the breast. *European Journal of Cancer (Oxford, England: 1990)* **40**, 336-341 (2004).

6. Pestalozzi BC*, et al.* Distinct Clinical and Prognostic Features of Infiltrating Lobular Carcinoma of the Breast: Combined Results of 15 International Breast Cancer Study Group Clinical Trials. *JCO* **26**, 3006-3014 (2008).

7. Rakha EA*, et al.* Invasive lobular carcinoma of the breast: response to hormonal therapy and outcomes. *European Journal of Cancer (Oxford, England: 1990)* **44**, 73-83 (2008).

8. Oesterreich S*, et al.* Clinicopathological Features and Outcomes Comparing Patients With Invasive Ductal and Lobular Breast Cancer. *JNCI: Journal of the National Cancer Institute* **114**, 1511-1522 (2022).

9. Desmedt C*, et al.* Immune Infiltration in Invasive Lobular Breast Cancer. *Journal of the National Cancer Institute* **110**, 768-776 (2018).

10. Tille J-C*, et al.* Tumor-infiltrating lymphocytes are associated with poor prognosis in invasive lobular breast carcinoma. *Mod Pathol* **33**, 2198-2207 (2020).

11. Costa A*, et al.* Fibroblast Heterogeneity and Immunosuppressive Environment in Human Breast Cancer. *Cancer Cell* **33**, 463-479 e410 (2018).

12. Pelon F*, et al.* Cancer-associated fibroblast heterogeneity in axillary lymph nodes drives metastases in breast cancer through complementary mechanisms. *Nat Commun* **11**, 1-20 (2020).

13. Sahai E*, et al.* A framework for advancing our understanding of cancer-associated fibroblasts. *Nat Rev Cancer* **20**, 174-186 (2020).

14. Mhaidly R, Mechta-Grigoriou F. Role of cancer-associated fibroblast subpopulations in immune infiltration, as a new means of treatment in cancer. *Immunological Reviews* **302**, 259-272 (2021).

15. Peltier A, Seban R-D, Buvat I, Bidard F-C, Mechta-Grigoriou F. Fibroblast heterogeneity in solid tumors: From single cell analysis to whole-body imaging. *Seminars in Cancer Biology* **86**, 262-272 (2022).

16. Chhabra Y, Weeraratna AT. Fibroblasts in cancer: Unity in heterogeneity. *Cell* **186**, 1580-1609 (2023).

17. Öhlund D*, et al.* Distinct populations of inflammatory fibroblasts and myofibroblasts in pancreatic cancer. *J Exp Med* **214**, 579-596 (2017).

18. Biffi G, Tuveson DA. Diversity and Biology of Cancer-Associated Fibroblasts. *Physiol Rev* **101**, 147-176 (2021).

19. Elyada E*, et al.* Cross-Species Single-Cell Analysis of Pancreatic Ductal Adenocarcinoma Reveals Antigen-Presenting Cancer-Associated Fibroblasts. *Cancer Discovery* **9**, 1102-1123 (2019).

20. Neuzillet C*, et al.* Inter- and intra-tumoural heterogeneity in cancer-associated fibroblasts of human pancreatic ductal adenocarcinoma. *The Journal of Pathology* **248**, 51-65 (2019).

21. Dominguez CX*, et al.* Single-Cell RNA Sequencing Reveals Stromal Evolution into LRRC15+ Myofibroblasts as a Determinant of Patient Response to Cancer Immunotherapy. *Cancer Discovery* **10**, 232-253 (2020).

22. Li H*, et al.* Reference component analysis of single-cell transcriptomes elucidates cellular heterogeneity in human colorectal tumors. *Nature Genetics* **49**, 708-718 (2017).

23. Givel A-M*, et al.* miR200-regulated CXCL12β promotes fibroblast heterogeneity and immunosuppression in ovarian cancers. *Nat Commun* **9**, 1-20 (2018).

24. Bartoschek M*, et al.* Spatially and functionally distinct subclasses of breast cancer-associated fibroblasts revealed by single cell RNA sequencing. *Nat Commun* **9**, 1-13 (2018).

25. Cremasco V*, et al.* FAP Delineates Heterogeneous and Functionally Divergent Stromal Cells in Immune-Excluded Breast Tumors. *Cancer Immunology Research* **6**, 1472-1485 (2018).

26. Friedman G*, et al.* Cancer-associated fibroblast compositions change with breast cancer progression linking the ratio of S100A4+ and PDPN+ CAFs to clinical outcome. *Nat Cancer* **1**, 692-708 (2020).

27. Kieffer Y*, et al.* Single-cell analysis reveals fibroblast clusters linked to immunotherapy resistance in cancer. *Cancer Discovery*, (2020).

28. Sebastian A*, et al.* Single-Cell Transcriptomic Analysis of Tumor-Derived Fibroblasts and Normal Tissue-Resident Fibroblasts Reveals Fibroblast Heterogeneity in Breast Cancer. *Cancers* **12**, 1307 (2020).

29. Wu SZ*, et al.* A single-cell and spatially resolved atlas of human breast cancers. *Nature Genetics* **53**, 1334-1347 (2021).

30. Foster DS*, et al.* Multiomic analysis reveals conservation of cancer-associated fibroblast phenotypes across species and tissue of origin. *Cancer Cell* **40**, 1392-1406.e1397 (2022).

31. Bonneau C*, et al.* A subset of activated fibroblasts is associated with distant relapse in early luminal breast cancer. *Breast Cancer Res* **22**, 76 (2020).

32. Cohen C*, et al.* WNT-dependent interaction between inflammatory fibroblasts and FOLR2+ macrophages promotes fibrosis in chronic kidney disease. *Nat Commun* **15**, 743 (2024).

33. Croizer H*, et al.* Deciphering the spatial landscape and plasticity of immunosuppressive fibroblasts in breast cancer. *Nat Commun* **15**, 2806 (2024).

34. Licaj M*, et al.* Residual ANTXR1+ myofibroblasts after chemotherapy inhibit anti-tumor immunity via YAP1 signaling pathway. *Nat Commun* **15**, 1312 (2024).

35. Denton AE, Roberts EW, Linterman MA, Fearon DT. Fibroblastic reticular cells of the lymph node are required for retention of resting but not activated CD8+ T cells. *Proc Natl Acad Sci U S A* **111**, 12139-12144 (2014).

36. Takahashi H*, et al.* Immunosuppressive activity of cancer-associated fibroblasts in head and neck squamous cell carcinoma. *Cancer Immunol Immunother* **64**, 1407-1417 (2015).

37. Ruhland MK*, et al.* Stromal senescence establishes an immunosuppressive microenvironment that drives tumorigenesis. *Nat Commun* **7**, 11762 (2016).

38. Yang X*, et al.* FAP Promotes Immunosuppression by Cancer-Associated Fibroblasts in the Tumor Microenvironment via STAT3-CCL2 Signaling. *Cancer Research* **76**, 4124-4135 (2016).

39. Zhang Y, Ertl HCJ. Depletion of FAP+ cells reduces immunosuppressive cells and improves metabolism and functions CD8+T cells within tumors. *Oncotarget* **7**, 23282-23299 (2016).

40. Cohen N*, et al.* Fibroblasts drive an immunosuppressive and growth-promoting microenvironment in breast cancer via secretion of Chitinase 3-like 1. *Oncogene* **36**, 4457-4468 (2017).

41. Wu SZ*, et al.* Stromal cell diversity associated with immune evasion in human triple-negative breast cancer. *The EMBO journal* **39**, e104063 (2020).

42. Magagna I*, et al.* CD73-Mediated Immunosuppression Is Linked to a Specific Fibroblast Population That Paves the Way for New Therapy in Breast Cancer. *Cancers* **13**, 5878 (2021).

43. Freeman P, Mielgo A. Cancer-Associated Fibroblast Mediated Inhibition of CD8+ Cytotoxic T Cell Accumulation in Tumours: Mechanisms and Therapeutic Opportunities. *Cancers* **12**, 2687 (2020).

44. Baker AT, Abuwarwar MH, Poly L, Wilkins S, Fletcher AL. Cancer-Associated Fibroblasts and T Cells: From Mechanisms to Outcomes. *J Immunol* **206**, 310-320 (2021).

45. Gorchs L, Kaipe H. Interactions between Cancer-Associated Fibroblasts and T Cells in the Pancreatic Tumor Microenvironment and the Role of Chemokines. *Cancers* **13**, 2995 (2021).

46. Biffi G*, et al.* IL1-Induced JAK/STAT Signaling Is Antagonized by TGFβ to Shape CAF Heterogeneity in Pancreatic Ductal Adenocarcinoma. *Cancer Discovery* **9**, 282-301 (2019).

47. Leader AM*, et al.* Single-cell analysis of human non-small cell lung cancer lesions refines tumor classification and patient stratification. *Cancer Cell* **39**, 1594-1609.e1512 (2021).

48. Nakagawa S*, et al.* Tumor microenvironment in invasive lobular carcinoma: possible therapeutic targets. *Breast Cancer Research and Treatment* **155**, 65-75 (2016).

49. Park CK, Jung WH, Koo JS. Expression of cancer-associated fibroblast-related proteins differs between invasive lobular carcinoma and invasive ductal carcinoma. *Breast Cancer Research and Treatment* **159**, 55-69 (2016).

50. Bassez A*, et al.* A single-cell map of intratumoral changes during anti-PD1 treatment of patients with breast cancer. *Nat Med* **27**, 820-832 (2021).

51. Pal B*, et al.* A single-cell RNA expression atlas of normal, preneoplastic and tumorigenic states in the human breast. *The EMBO journal* **40**, e107333 (2021).

52. Hofer I*, et al.* An Extracellular Matrix-Producing Subset of Cancer-Associated Fibroblasts Drives Chemoresistance in Breast Cancer via SRC Activation and G0S2 Upregulation. *Cancer Res*, (2025).

53. Mahmoud SM*, et al.* Tumor-infiltrating CD8+ lymphocytes predict clinical outcome in breast cancer. *J Clin Oncol* **29**, 1949-1955 (2011).

54. Ali HR*, et al.* Association between CD8+ T-cell infiltration and breast cancer survival in 12,439 patients. *Ann Oncol* **25**, 1536-1543 (2014).

55. Savas P*, et al.* Single-cell profiling of breast cancer T cells reveals a tissue-resident memory subset associated with improved prognosis. *Nat Med* **24**, 986-993 (2018).

56. Onkar S*, et al.* Immune landscape in invasive ductal and lobular breast cancer reveals a divergent macrophage-driven microenvironment. *Nat Cancer* **4**, 516-534 (2023).

57. Gueguen P*, et al.* Contribution of resident and circulating precursors to tumor-infiltrating CD8+ T cell populations in lung cancer. *Sci Immunol* **6**, eabd5778 (2021).

58. Mami-Chouaib F*, et al.* Resident memory T cells, critical components in tumor immunology. *J Immunother Cancer* **6**, 87 (2018).

59. Edwards J*, et al.* CD103+ Tumor-Resident CD8+ T Cells Are Associated with Improved Survival in Immunotherapy-Naïve Melanoma Patients and Expand Significantly During Anti-PD-1 Treatment. *Clin Cancer Res* **24**, 3036-3045 (2018).

60. Byrne A*, et al.* Tissue-resident memory T cells in breast cancer control and immunotherapy responses. *Nat Rev Clin Oncol* **17**, 341-348 (2020).

61. Corgnac S*, et al.* CD103+CD8+ TRM Cells Accumulate in Tumors of Anti-PD-1-Responder Lung Cancer Patients and Are Tumor-Reactive Lymphocytes Enriched with Tc17. *Cell Rep Med* **1**, 100127 (2020).

62. Virassamy B*, et al.* Intratumoral CD8+ T cells with a tissue-resident memory phenotype mediate local immunity and immune checkpoint responses in breast cancer. *Cancer Cell* **41**, 585-601.e588 (2023).

63. Shields BD*, et al.* Loss of E-Cadherin Inhibits CD103 Antitumor Activity and Reduces Checkpoint Blockade Responsiveness in Melanoma. *Cancer Research* **79**, 1113-1123 (2019).

64. Skon CN, Lee J-Y, Anderson KG, Masopust D, Hogquist KA, Jameson SC. Transcriptional downregulation of S1pr1 is required for the establishment of resident memory CD8+ T cells. *Nat Immunol* **14**, 1285-1293 (2013).

65. Quinn E, Hawkins N, Yip YL, Suter C, Ward R. CD103+ intraepithelial lymphocytes--a unique population in microsatellite unstable sporadic colorectal cancer. *European Journal of Cancer (Oxford, England: 1990)* **39**, 469-475 (2003).

66. Webb JR, Milne K, Watson P, Deleeuw RJ, Nelson BH. Tumor-infiltrating lymphocytes expressing the tissue resident memory marker CD103 are associated with increased survival in high-grade serous ovarian cancer. *Clin Cancer Res* **20**, 434-444 (2014).

67. Djenidi F*, et al.* CD8+CD103+ tumor-infiltrating lymphocytes are tumor-specific tissue-resident memory T cells and a prognostic factor for survival in lung cancer patients. *J Immunol* **194**, 3475-3486 (2015).

68. Wang B*, et al.* CD103+ Tumor Infiltrating Lymphocytes Predict a Favorable Prognosis in Urothelial Cell Carcinoma of the Bladder. *J Urol* **194**, 556-562 (2015).

69. Wang Z-Q, Milne K, Derocher H, Webb JR, Nelson BH, Watson PH. CD103 and Intratumoral Immune Response in Breast Cancer. *Clin Cancer Res* **22**, 6290-6297 (2016).

70. Kumar V*, et al.* Single-Cell Atlas of Lineage States, Tumor Microenvironment, and Subtype-Specific Expression Programs in Gastric Cancer. *Cancer Discov* **12**, 670-691 (2022).

71. Van Baelen K*, et al.* Current and future diagnostic and treatment strategies for patients with invasive lobular breast cancer. *Ann Oncol*, S0923-7534(0922)01167-X (2022).

72. Finak G*, et al.* Stromal gene expression predicts clinical outcome in breast cancer. *Nat Med* **14**, 518-527 (2008).

73. Whittard JD*, et al.* E-cadherin is a ligand for integrin alpha2beta1. *Matrix Biol* **21**, 525-532 (2002).

74. Shafraz O, Xie B, Yamada S, Sivasankar S. Mapping transmembrane binding partners for E-cadherin ectodomains. *Proc Natl Acad Sci U S A* **117**, 31157-31165 (2020).

75. Aluwihare P*, et al.* Mice that lack activity of alphavbeta6- and alphavbeta8-integrins reproduce the abnormalities of Tgfb1- and Tgfb3-null mice. *J Cell Sci* **122**, 227-232 (2009).

76. Shi M*, et al.* Latent TGF-β structure and activation. *Nature* **474**, 343-349 (2011).

77. Zhao M*, et al.* Targeting fibrosis: mechanisms and clinical trials. *Sig Transduct Target Ther* **7**, 1-21 (2022).

78. Vaughan MB, Howard EW, Tomasek JJ. Transforming Growth Factor-β1 Promotes the Morphological and Functional Differentiation of the Myofibroblast. *Experimental Cell Research* **257**, 180-189 (2000).

79. Calon A*, et al.* Dependency of Colorectal Cancer on a TGF-β-Driven Program in Stromal Cells for Metastasis Initiation. *Cancer Cell* **22**, 571-584 (2012).

80. Krishnamurty AT*, et al.* LRRC15+ myofibroblasts dictate the stromal setpoint to suppress tumour immunity. *Nature* **611**, 148-154 (2022).

81. Davidson S*, et al.* Fibroblasts as immune regulators in infection, inflammation and cancer. *Nat Rev Immunol* **21**, 704-717 (2021).

82. Caligiuri G, Tuveson DA. Activated fibroblasts in cancer: Perspectives and challenges. *Cancer Cell* **41**, 434-449 (2023).

83. Salmon H*, et al.* Matrix architecture defines the preferential localization and migration of T cells into the stroma of human lung tumors. *J Clin Invest* **122**, 899-910 (2012).

84. Mariathasan S*, et al.* TGFβ attenuates tumour response to PD-L1 blockade by contributing to exclusion of T cells. *Nature* **554**, 544-548 (2018).

85. Nicolas-Boluda A*, et al.* Tumor stiffening reversion through collagen crosslinking inhibition improves T cell migration and anti-PD-1 treatment. *eLife* **10**, e58688 (2021).

86. Raskov H, Orhan A, Christensen JP, Gögenur I. Cytotoxic CD8+ T cells in cancer and cancer immunotherapy. *Br J Cancer* **124**, 359-367 (2021).

87. Heindl A, Sestak I, Naidoo K, Cuzick J, Dowsett M, Yuan Y. Relevance of Spatial Heterogeneity of Immune Infiltration for Predicting Risk of Recurrence After Endocrine Therapy of ER+ Breast Cancer. *Journal of the National Cancer Institute* **110**, (2018).

88. Gao Z-H, Li C-X, Liu M, Jiang J-Y. Predictive and prognostic role of tumour-infiltrating lymphocytes in breast cancer patients with different molecular subtypes: a meta-analysis. *BMC Cancer* **20**, 1150 (2020).

89. Egelston CA*, et al.* Tumor-infiltrating exhausted CD8+ T cells dictate reduced survival in premenopausal estrogen receptor-positive breast cancer. *JCI Insight* **7**, e153963 (2022).

90. Makhlouf S*, et al.* Evaluation of tumour infiltrating lymphocytes in luminal breast cancer using artificial intelligence. *Br J Cancer*, (2023).

91. Dunbier AK*, et al.* Molecular profiling of aromatase inhibitor-treated postmenopausal breast tumors identifies immune-related correlates of resistance. *Clin Cancer Res* **19**, 2775-2786 (2013).

92. Skriver SK, Jensen M-B, Knoop AS, Ejlertsen B, Laenkholm A-V. Tumour-infiltrating lymphocytes and response to neoadjuvant letrozole in patients with early oestrogen receptor-positive breast cancer: analysis from a nationwide phase II DBCG trial. *Breast Cancer Res* **22**, 46 (2020).

93. Rothenberger NJ, Somasundaram A, Stabile LP. The Role of the Estrogen Pathway in the Tumor Microenvironment. *Int J Mol Sci* **19**, 611 (2018).

94. Moisand A, Madéry M, Boyer T, Domblides C, Blaye C, Larmonier N. Hormone Receptor Signaling and Breast Cancer Resistance to Anti-Tumor Immunity. *Int J Mol Sci* **24**, 15048 (2023).

95. Li Y*, et al.* Unlocking the therapeutic potential of the NKG2A-HLA-E immune checkpoint pathway in T cells and NK cells for cancer immunotherapy. *J Immunother Cancer* **12**, (2024).

96. Torrisi R*, et al.* Preoperative bevacizumab combined with letrozole and chemotherapy in locally advanced ER- and/or PgR-positive breast cancer: clinical and biological activity. *Br J Cancer* **99**, 1564-1571 (2008).

97. Dickler MN*, et al.* Phase III Trial Evaluating Letrozole As First-Line Endocrine Therapy With or Without Bevacizumab for the Treatment of Postmenopausal Women With Hormone Receptor-Positive Advanced-Stage Breast Cancer: CALGB 40503 (Alliance). *J Clin Oncol* **34**, 2602-2609 (2016).

98. Voorwerk L*, et al.* PD-L1 blockade in combination with carboplatin as immune induction in metastatic lobular breast cancer: the GELATO trial. *Nat Cancer* **4**, 535-549 (2023).

99. Djerroudi L*, et al.* Molecular and Clinical Portrait of HER2-low Invasive Lobular Carcinomas. *Mod Pathol* **37**, 100463 (2024).

100. Djerroudi L*, et al.* E-Cadherin Mutational Landscape and Outcomes in Breast Invasive Lobular Carcinoma. *Mod Pathol* **37**, 100570 (2024).

101. Salgado R*, et al.* The evaluation of tumor-infiltrating lymphocytes (TILs) in breast cancer: recommendations by an International TILs Working Group 2014. *Ann Oncol* **26**, 259-271 (2015).

102. Hendry S*, et al.* Assessing Tumor-infiltrating Lymphocytes in Solid Tumors: A Practical Review for Pathologists and Proposal for a Standardized Method From the International Immunooncology Biomarkers Working Group: Part 1: Assessing the Host Immune Response, TILs in Invasive Breast Carcinoma and Ductal Carcinoma In Situ, Metastatic Tumor Deposits and Areas for Further Research. *Adv Anat Pathol* **24**, 235-251 (2017).

103. Wolff AC*, et al.* Human Epidermal Growth Factor Receptor 2 Testing in Breast Cancer: American Society of Clinical Oncology/College of American Pathologists Clinical Practice Guideline Focused Update. *Journal of Clinical Oncology: Official Journal of the American Society of Clinical Oncology* **36**, 2105-2122 (2018).

104. Allison KH*, et al.* Estrogen and Progesterone Receptor Testing in Breast Cancer: American Society of Clinical Oncology/College of American Pathologists Guideline Update. *Arch Pathol Lab Med* **144**, 545-563 (2020).

105. Franchet C*, et al.* [2021 update of the GEFPICS' recommendations for HER2 status assessment in invasive breast cancer in France]. *Ann Pathol* **41**, 507-520 (2021).

106. Balaton AL*, et al.* [Recommendations for the immunohistochemical evaluation of hormone receptors on paraffin sections of breast cancer. Study Group on Hormone Receptors using Immunohistochemistry FNCLCC/AFAQAP. National Federation of Centres to Combat Cancer/French Association for Quality Assurance in Pathology]. *Ann Pathol* **16**, 144-148 (1996).

107. Zafrani B*, et al.* High sensitivity and specificity of immunohistochemistry for the detection of hormone receptors in breast carcinoma: comparison with biochemical determination in a prospective study of 793 cases. *Histopathology* **37**, 536-545 (2000).

108. Bankhead P*, et al.* QuPath: Open source software for digital pathology image analysis. *Sci Rep* **7**, 16878 (2017).

109. Chu T, Wang Z, Pe'er D, Danko CG. Cell type and gene expression deconvolution with BayesPrism enables Bayesian integrative analysis across bulk and single-cell RNA sequencing in oncology. *Nat Cancer* **3**, 505-517 (2022).

110. Cancer Genome Atlas N. Comprehensive molecular portraits of human breast tumours. *Nature* **490**, 61-70 (2012).

111. Boelens MC*, et al.* PTEN Loss in E-Cadherin-Deficient Mouse Mammary Epithelial Cells Rescues Apoptosis and Results in Development of Classical Invasive Lobular Carcinoma. *Cell Rep* **16**, 2087-2101 (2016).

112. Huijbers IJ*, et al.* Rapid target gene validation in complex cancer mouse models using re-derived embryonic stem cells. *EMBO Mol Med* **6**, 212-225 (2014).

113. Houthuijzen JM*, et al.* CD26-negative and CD26-positive tissue-resident fibroblasts contribute to functionally distinct CAF subpopulations in breast cancer. *Nat Commun* **14**, 183 (2023).

114. Newman AM*, et al.* Determining cell type abundance and expression from bulk tissues with digital cytometry. *Nat Biotechnol* **37**, 773-782 (2019).

115. Wellenstein MD*, et al.* Loss of p53 triggers WNT-dependent systemic inflammation to drive breast cancer metastasis. *Nature* **572**, 538-542 (2019).

ACKNOWLEDGEMENTS

We would like to thank Profs. Christine Desmedt (KU Leuven), Steffi Oesterreich and Adrian Lee (University of Pittsburgh) and Patrick Derksen (Utrecht University) for fruitful discussions within the frame of the ELBCC (European Lobular Breast Cancer Consortium) that inspired our work. We are grateful to institute Curie colleagues, including Charlotte Martinat and Khadidja Klouch for collecting clinical data of the patients (SIRIC, INCa-DGOS-4654); Jean-Christophe Tille and Amel Bendali for their help for pathological review of the slides; Laetitia Lesage, Gabriel Champenois and André Nicolas for their help at the experimental pathology platform and Coralie Guerin and Lea Guyonnet at the cytometry core.

FUNDINGS

F.M.-G. and G.G. are permanent scientists at Inserm. R.M. was supported by the Foundation de France (00119142/WB−2021-36276) and Y.K. by the Institut National du Cancer and INCa (CAFHeros, INCa-16101). The experimental work was supported by grants from the Ligue Nationale Contre le Cancer (LNCC, Labelisation), Inserm, INCa (CAFHeros INCa-16101; ChemoCAF, INCa-16086), ITMO Cancer of Aviesan (2021-2030 cancer control strategy framework, Pre-Caution), SIGN'it 2019 from the Foundation ARC, the European TRANSCAN-3 ERA-NET and the ARC Foundation for the CHRYSALIS funding (ARCPARTN-TRANS2022080005422) and Magnolia (INCa-16786), as well as the MSDAvenir program HoLOGRAM and BC-DigitalPath. L.D. thanks La Ligue contre le Cancer, institut Servier and Foundation ARC for their support. This work has been supported by a Ruban Rose grant attributed to A.V.-S. This work is presented on behalf of the IHU sein working group; the IHU Institute of Women's Cancer is funded by the Agence Nationale de la Recherche (ANR) in the frame of France 2030 (grant number ANR-23-IHU-006). We are also grateful to the ANR for the funding of the CASSIOPEIA RHU (ANR-21-RHUS-0002) program as part of the PIA France 2030. The ICGex NGS platform was supported by the ANR-10-EQPX-03 (Equipex) and ANR-10-INBS-09-08 (France Genomic Consortium) grants. F.M.-G. acknowledges the French "Pink Ribbon" association and the "Simone and Cino del Duca Foundation" for attribution of their respective Grand Prix, as well as the FRM for the Rozen Prize and the LNCC for the Duquesne Price and the association "Christelle Bouillot". F.M.-G. is very grateful to all her funders for providing support throughout the years. The graphical abstract in Fig. 6 was created with Biorender.com.

AUTHOR CONTRIBUTIONS

F.M.-G., A.V.-S. and L.D. conceived the entire project and designed the concept of experiments. L.D., I.D. and R.M. performed experiments and acquired data, together with G.G., M.C., C.R. and R.L., Y.K., V.S., H.C. and L.D. performed all bioinformatic and statistical analyses. C.B., V.R. and L.D. performed genetic analyses. A.V.-S. built cohorts of patients, provided human samples and expertise in pathology analyses, together with L.D. and F.-C.B. E.L., C.M. and K.C. contributed to building and characterizing at the clinical level the retrospective or the prospective cohorts of patients with ILC. Moreover, L.F. and A.G. collected clinical data. J.H., P.K., J.J. performed the mouse transcriptomic analyses. F.M.-G. and A.V.-S. supervised the entire project and wrote the paper with L.D., Y.K. and R.M., with suggestions from all authors.

COMPETING INTERESTS

F.M.-G. and A.V.-S received research support from Roche, Institut Roche and the MSD Foundation. L.D. received research mobility support from Institut Servier. F.-C.B reports research funding from GE Healthcare, Menarini Silicon Biosystems, Merck KGaA, MSD, Natera, Novartis, Personalis, Pfizer, Prolynx, Roche, SAGADx and Tempus; has served on advisory boards for AstraZeneca, Carrick Therapeutics, Daiichi Sankyo, Hengrui, Inatherys, Lilly, Menarini Silicon Biosystems, Novartis, Pfizer, Relay Therapeutics, Roche and Tempus; and has received speaker honoraria and travel support from AstraZeneca, Daiichi Sankyo, Lilly, Novartis, Pfizer and Roche. Other authors declare no potential conflict of interest.

FIGURE LEGENDS

Figure 1. Invasive lobular carcinomas (ILCs) are enriched in FAP+ inflammatory CAF (FAP+ iCAF) compared to invasive carcinomas of no special type (IC-NSTs)

(**A**) Representative immunohistochemistry for SMA (myofibroblast marker), FAP (FAP+ CAF / CAF-S1 marker), ANTXR1 (FAP+ myCAF marker), and SDC1 (ECM-myCAF marker) in ER+ IC-NSTs (left) and ER+ ILCs (right). Scale bars represent 100 µm for ER+ IC-NST images and 200 µm for ER+ ILC images, except in magnified insets where scale bars correspond to 20 µm. (**B**) Boxplot (top) and density plot (bottom) of SMA H-score in ER+ IC-NSTs (N=77) *versus* ER+ ILCs (N=158). P-value from Mann-Whitney test. (**C**) Boxplot (top) of FAP H-score in ER+ IC-NSTs *versus* ILCs. P-value from Mann-Whitney test. Scatter plot (bottom) showing the correlation between SMA and FAP H-scores (N=77 ER+ IC-NSTs and 158 ILCs). P-value from Pearson's correlation test. (**D**) Boxplots of ANTXR1 (top) and SDC1 (bottom) H-scores in ER+ IC-NSTs *versus* ILCs. P-values from Mann-Whitney test. In boxplots (**B-D**), the center line indicates the median, the box spans the first to third quartiles (IQR), and whiskers extend to 1.5 × IQR. (**E**) Proportions (%) of FAP+ CAF clusters among total FAP+ CAF assessed by the combined IHC analysis of specific FAP+ CAF cluster markers in ER+ IC-NSTs and ILCs. Only cases with FAP H-score >1st quartile were retained for analysis, and enrichment of specific FAP+ CAF clusters was determined based on ANTXR1 and SDC1 H-scores (Gaussian mixture models were used to determine thresholds between low and high H-scores for FAP+ CAF cluster markers). P-value from Fisher's Exact test. (**F**) UMAP of scRNA-seq data from 11,384 FAP+ CAF showing the distribution of FAP+ CAF clusters in ER+ ILCs (N=6) and ER+ IC-NSTs (N=15). (**G**) Proportions of FAP+ CAF clusters among total FAP+ CAF assessed by deconvolution of bulk RNA-seq data from ER+ ILCs (Institut Curie ILC retrospective series, N=234), ER+ IC-NSTs (TCGA cohort, N=446), and TN IC-NSTs (Institut Curie SCANDARE cohort, N=78). P-value from Fisher's Exact test. (**H**) Proportions of FAP+ CAF clusters among total FAP+ CAF assessed by deconvolution of RNA-seq data in each individual case from the ER+ ILC retrospective series (N=234). (**I**) Same as in (**G**) with ILC cases stratified by histological subtype (classic, N=159 or non-classic, N=75) and tumor cellularity (high, N=98 or low, N=136). P-value from Fisher's Exact test. (**J**) Proportions of FAP+ CAF clusters among total FAP+ CAF assessed by combined IHC analysis of FAP+ CAF cluster markers in ER+ IC-NSTs and ER+ ILC cases stratified by histological subtypes (classic or non-classic) and tumor cellularity (high or low). P-value from Fisher's Exact test. (**K**) Proportions of FAP+ iCAF and myCAF among total FAP+ CAF, assessed using scRNA-seq data from CDH1-deficient mouse models (WEPtn and WEE545K) and CDH1-proficient controls (WPtn and

WE545K). P-value from Fisher's Exact test. Data are mean +/- SEM (n = 17 mice) (**A-E, J**) Institut Curie IHC retrospective series (N=77 ER+ IC-NSTs and 158 ER+ ILCs); (**F**) Institut Curie prospective series of ER+ ILC (N=6). All statistical tests were two-sided. Source data are provided as a Source Data file.

Figure 2. The E-cadherin pathway is involved in the differentiation of Detox-iCAF into ECM-myCAF

(**A**) CellChat dominant sender and receiver plot showing incoming interaction strength according to outgoing interaction strength for each cell type identified in the single-cell cellular Atlas considering all signaling pathways in ER+ IC-NSTs (top) and ILCs (bottom). The size of each circle corresponds to the total number of significant interactions, colored by cell type. (**B**) Same as in (**A**) focused on the E-cadherin-dependent pathway. (**C**) Chord diagram for inferred CDH1-ITGB1 interactions from cancer cells to all other cell types identified in the cellular Atlas in ER+ IC-NSTs (top) and ILCs (bottom). Edge width represents the communication probability computed by CellChat. (**D**) Flow cytometry plots showing FAP+ CAF cluster-specific surface markers in sorted primary FAP+ CAF from breast cancer patients. (**E**) Up, Bar plots showing the fractions of FAP+ iCAF (ANTXR1-, in yellow) and FAP+ myCAF (ANTXR1+, in red) clusters among FAP+ CAF after 48h of culture of FAP+ iCAF alone, or with ER+ breast cancer cell lines (MCF7 or T47D) transfected either with siCTRL or with 2 different siRNA targeting *CDH1* (siCDH1#1 and siCDH1#2). Data are mean +/- SEM (n = 3). Bottom, Same as Up for each FAP+ CAF cluster. Respective identity of each cluster is based on specific markers assessed by flow cytometry: ECM-myCAF (ANTXR1+ SDC1+ LAMP5-, red); TGFβ-myCAF (ANTXR1+ SDC1+ LAMP5+, dark green); IL-iCAF (ANTXR1- DLK1+ GPC3-, light green); Detox-iCAF (ANTXR1- DLK1+/- GPC3+, yellow) and IFNγ-iCAF (ANTXR1- DLK1- GPC3- CD74+, blue). Data are mean +/- SEM (n = 3). P-values from two-sided Fisher's Exact test. (**F, G**) Same as (**D, E**) after 48h of culture of FAP+ iCAF alone, or of co-culture of FAP+ iCAF transfected either with siCtrl or with 2 specific siRNA targeting *ITGB1* (siITGB1#1 and siITGB1#2) with ER+ breast cancer cell lines (MCF7 or T47D). Data are mean +/- SEM (n = 3). (**A-C**) Institut Curie prospective series of ER+ ILC (N=6). Source data are provided as a Source Data file.

Figure 3. The spatial organization of tumor-infiltrating lymphocytes (TILs) is associated with FAP+ iCAF content

(**A**) Representative images (HES) of ILC cases with infiltrating (top) or margin-predominant (bottom) spatial organization patterns of TILs. (**B**) Boxplots of H-scores for SMA (top, left), FAP

(top, right), ANTXR1 (bottom, left), and SDC1 (bottom, right) in ER+ ILCs with infiltrating (N=80) *versus* margin-predominant (N=46) TIL patterns. P-values from Mann-Whitney test. Center line indicates the median, the box spans the first to third quartiles (IQR), and whiskers extend to 1.5 × IQR. (**C**) Bar plot showing the proportions of FAP+ CAF clusters among total FAP+ CAF assessed by the combined IHC analysis of specific FAP+ CAF cluster markers in ER+ ILCs with infiltrating (N=44) *versus* margin-predominant (N=33) TIL patterns. P-value from Fisher's Exact test. (**D**) Boxplots showing the proportions of each FAP+ CAF cluster among all cell types identified by deconvolution of bulk RNA-seq data from ER+ ILCs with infiltrating (N=118) *versus* margin-predominant (N=72) TIL patterns using the scRNA-seq-based cellular Atlas. P-values from Mann-Whitney test. Center line indicates the median, the box spans the first to third quartiles (IQR), and whiskers extend to 1.5 × IQR. (**E**) Bar plot showing the percentages (%) of migration of CD8+ T lymphocytes after 24hrs of transwell culture in several conditions: alone (CD8+ T cells alone); with MCF7 breast cancer cells transfected either with a control siRNA (MCF7 *siCTRL*) or with 2 different siRNA targeting *CDH1* (MCF7 siCDH1#1 and siCDH1#2) ; with FAP+ iCAF; with ECM-myCAF; with both MCF7 breast cancer cells (siCTRL siCDH1#1 and siCDH1#2) and FAP+ iCAF or ECM-myCAF. Data are mean +/- SEM (n = 3). P-values from Mann-Whitney test. (**F**) Same as (**E**) with T47D breast cancer cells. (**G, H**) Same as (**E, F**) after co-culture of MCF7 (**G**) or T47D (**H**) cancer cells with FAP+ iCAF transfected either with *siCTRL* or with 2 different siRNA targeting *ITGB1* (*siITGB1#1* and *siITGB1#2*). Data are mean +/- SEM (n = 3). P-values from Mann-Whitney test. (**B, C)** Institut Curie IHC retrospective series (ER+ ILC cases with detectable TILs only, N=126); **(D**) Institut Curie ILC retrospective series (ER+ ILC cases with detectable TILs only, N=190). All statistical tests were two-sided. Source data are provided as a Source Data file.

Figure 4. TIL content and spatial organization are associated with poor prognosis in patients with ILC

(**A**) Kaplan-Meier curves showing overall survival (OS, left) and distant metastasis-free interval (DMFI, right) of ILC patients (N=251) stratified by TIL content (< or >=5%) and spatial organization pattern (infiltrating or margin-predominant). P-values from Log-rank test. (**B**) Univariate Cox analysis of OS (left) and DMFI (right) for ILC patients (N=251) stratified according to TIL content and spatial organization patterns (<5% or ≥5%; infiltrating or margin-predominant). Rectangles indicate hazard ratios (HR); horizontal bars show 95% confidence intervals. *p < 0.05; **p < 0.01; ***p < 0.001 (two-sided univariate Cox proportional hazards models, no correction for multiple testing). (**C**) Multivariate Cox analysis of OS (left) and DMFI (right) performed with clinicopathological variables that were significantly associated with survival in univariate analysis,

including age (<50, 50-64, >=65), grade (1-2, 3), pathological primary tumor (pT=1-3), positive nodes (pN=0-3), lymphovascular invasion (LVI: no, yes), progesterone receptor (PR) status (positive, negative), TIL content and spatial distribution pattern (<5% or >=5%; infiltrating or margin-predominant). Rectangles indicate hazard ratios (HR); horizontal bars show 95% confidence intervals. *p < 0.05; **p < 0.01; ***p < 0.001 (two-sided multivariate Cox proportional hazards models adjusted for covariates). (**D**) Heatmap and clustering of samples (columns) from ILC patients (N=251) showing 4 subgroups of ILC patients (TME class 1: N=50; TME class 2: N=90; TME class 3: N=67; TME class 4: N=44). (**A-D**) Institut Curie ILC retrospective series (N=251). Source data are provided as a Source Data file.

Figure 5. E-cadherin/*CDH1* loss induces immune escape due to a lack of retention, interaction and activation of ITGAE-expressing resident memory CD8+ T lymphocytes

(**A**) UMAP of scRNA-seq data from lymphoid cells (including 15,605 CD8+ T lymphocytes), showing the distribution of lymphoid cell clusters in ER+ ILCs (N=6) (left) and ER+ IC-NSTs (N=15) (right). (**B**) Bar plot showing the proportion of CD8+ T cell clusters among total CD8+ T cells from scRNA-seq data. P-value from Fisher's Exact test. (**C**) UMAPs showing expression of the *ITGAE* gene across lymphoid clusters (left) and expression of CD8+ T resident memory signature from [55] across lymphoid clusters (right). (**D**) Violin plot showing expression of the CD8+ T resident memory signature across CD8+ T cell clusters (left) and between ER+ IC-NSTs and ER+ ILCs (right). P-value from Mann-Whitney test. (**E**) Bar plot showing the proportions of CD8+ T cell clusters among total CD8+ T cells assessed by deconvolution of bulk RNA-seq data from ER+ ILCs (Institut Curie ILC retrospective series, N=234) and ER+ IC-NSTs (TCGA cohort, N=446). Only cases with at least 5% of lymphoid cells detected were included in this analysis (N=170 ILCs and N=13 IC-NSTs). P-value from Fisher's Exact test. (**F**) Boxplot showing the ratio of CD8-GZMH / CD8-KLF2 T lymphocytes estimated by deconvolution of bulk RNA-seq data from ER+ ILCs (Institut Curie retrospective series, N=234) *versus* ER+ IC-NSTs (TCGA, N=446). P-value from Mann-Whitney test. (**G**) Boxplot showing the number of ITGAE/CD103+ immune cells per mm^2 assessed by IHC in ER+ IC-NSTs (N=77) *versus* classic E-cadherin- ILCs (N=47). P-value from Mann-Whitney test. In boxplots (**F, G**), the center line indicates the median, the box spans the first to third quartiles (IQR), and whiskers extend to 1.5 × IQR. (**H**) Bar plots showing expression of IFNγ (assessed by FACS) by CD8+ CD103+ (left) or CD8+ CD103- T lymphocytes (right) cultured for 24h alone or co-cultured with breast cancer cell lines (MCF7 or T47D) transfected either with *siCTRL* or with 2 different siRNA targeting *CDH1* (*siCDH1#1* and *siCDH1#2*). Data are mean +/- SEM (n=6). P-values from Mann-Whitney test. (**I**) Same as (**H**) for

Perforin. (**J-L**) scRNA-seq data from gastric tumor (n=8,271 cells; N= 25 samples from 20 patients). (**J**) Bar plot showing the proportions of FAP+ CAF clusters among total FAP+ CAF from intestinal (n=6,592 cells) compared to diffuse (n=1,679 cells) subtypes of gastric cancers. P-value from Fisher's Exact test. (**K**) Same as (J) for the proportions of CD8+ T cell clusters among total CD8+ T lymphocytes. (**L**) Violin plot showing expression of the CD8+ T resident memory (TRM) signature in intestinal and diffuse gastric cancers. P-value from Mann-Whitney test. (**A-D**) Institut Curie prospective series of ER+ ILCs (N=6); (**E, F**) Institut Curie ILC retrospective series (ER+ ILC cases only, N=234), and ER+ IC-NSTs from TCGA (N=446); (**G**) Institut Curie IHC retrospective series (N= 77 ER+ IC-NSTs and 47 classic E-cadherin- ILCs) ; (**J-L**) Gastric cancer public dataset [70]. All statistical tests were two-sided. Source data are provided as a Source Data file.

Figure 6. Schematic overview of TME remodeling upon E-cadherin loss (A) and TME classification of ILC with therapeutic opportunities (B)

(A) The tumor microenvironment (TME) of ILC exhibits distinct characteristics driven by E-cadherin/*CDH1* loss in cancer cells. In this paper, we describe the composition of CAF populations and immune cell subsets, as well as their reciprocal interactions with tumor cells, in ILC compared to IC-NST. To achieve this, we combined immunohistochemical analyses, single-cell RNA sequencing, deconvolution of bulk RNA-seq from large ILC and IC-NST datasets, functional assays using primary cells, and analyses from *in vivo* mouse models. In IC-NST, E-cadherin-positive (CDH1+) cancer cells promote the differentiation of Detox-iCAF into ECM-myCAF, likely through heterologous interaction with the integrin-β1/ITGB1 receptor at the surface of CAF. Additionally, E-cadherin interacts with another integrin, αE-integrin/ITGAE, to facilitate the retention and cytotoxic activity of the CD8+ tissue-resident memory T cells (TRM), a subset of CD8+ T lymphocytes which is a key component of anti-tumor immunity. In contrast, in ILC, E-cadherin/*CDH1* loss prevents the differentiation of Detox-iCAF into ECM-myCAF, leading to Detox-iCAF accumulation. In turn, Detox-iCAF enrichment in ILC induces a spatial reorganization of tumor-infiltrating lymphocytes (TILs), promoting their accumulation in the tumor core. E-cadherin/CDH1 loss (CDH1-) in ILC cancer cells disrupts their interactions with TRM cells, thereby preventing retention and activation of ITGAE-expressing TRM cells, and promoting accumulation of CD8+ T lymphocytes in a precursor (CD8-KLF2) state, reducing their differentiation into cytotoxic CD8+ T cells. The altered TIL phenotype promotes immune escape and explains -at least in part- their poor prognostic impact in patients with ILC.

Hence, our study uncovers reciprocal interactions between *CDH1*-inactivated cancer cells, iCAF and CD8+ TRM, providing insight into the underlying mechanism associated with the stromal reaction in ILC and revealing why TILs are associated with a poor prognosis in patients with ILC**.** Created in BioRender. Mechta-grigoriou, F. (2026) https://BioRender.com/9iywa0l. (**B**) Detailed characterization of TME heterogeneity in ILC, divided into four TME classes (referred to as TEDI TME classes) with specific cellular composition, histological features, prognostic outcomes and therapeutic opportunities (as shown in **Fig. 4D**). TME class 1 (**T**GFβ/Wound-myCAF-enriched) is associated with favorable prognosis and may be eligible for therapeutic de-escalation. TME class 2 (**E**CM/IFNαβ-myCAF-enriched) is enriched in TREM2+/SPP1+ tumor-associated macrophages (TAM), representing a potential therapeutic target. TME class 3 (**D**etox-iCAF-enriched) contains NKG2A+ NK cells, targetable for anti-tumor effects, as well as endothelial cells, suggesting possible efficacy of anti-angiogenic therapy. TME class 4 (**I**mmune-cell-enriched) may benefit from anti-inflammatory strategies to overcome endocrine resistance and could be considered for immunotherapy targeting non-CD8 cells to bypass CD8-related immune escape mechanisms; a subset of these tumors (E-cadherin+) may also still respond to conventional immunotherapy. Created in BioRender. Mechta-grigoriou, F. (2026) https://BioRender.com/56wo0ib.

Editorial summary

Features of the stroma and immune infiltrate in patients with invasive lobular breast carcinoma (ILC) have been associated with poor prognosis. Here the authors report that E-cadherin loss in ILC cancer cells influences cancer associated fibroblast differentiation and spatial organization of tumor-infiltrating lymphocytes, resulting in immune escape and poor prognosis.

Peer Review Information: *Nature Communications* thanks Yunshun Chen and the other, anonymous, reviewer(s) for their contribution to the peer review of this work. A peer review file is available.

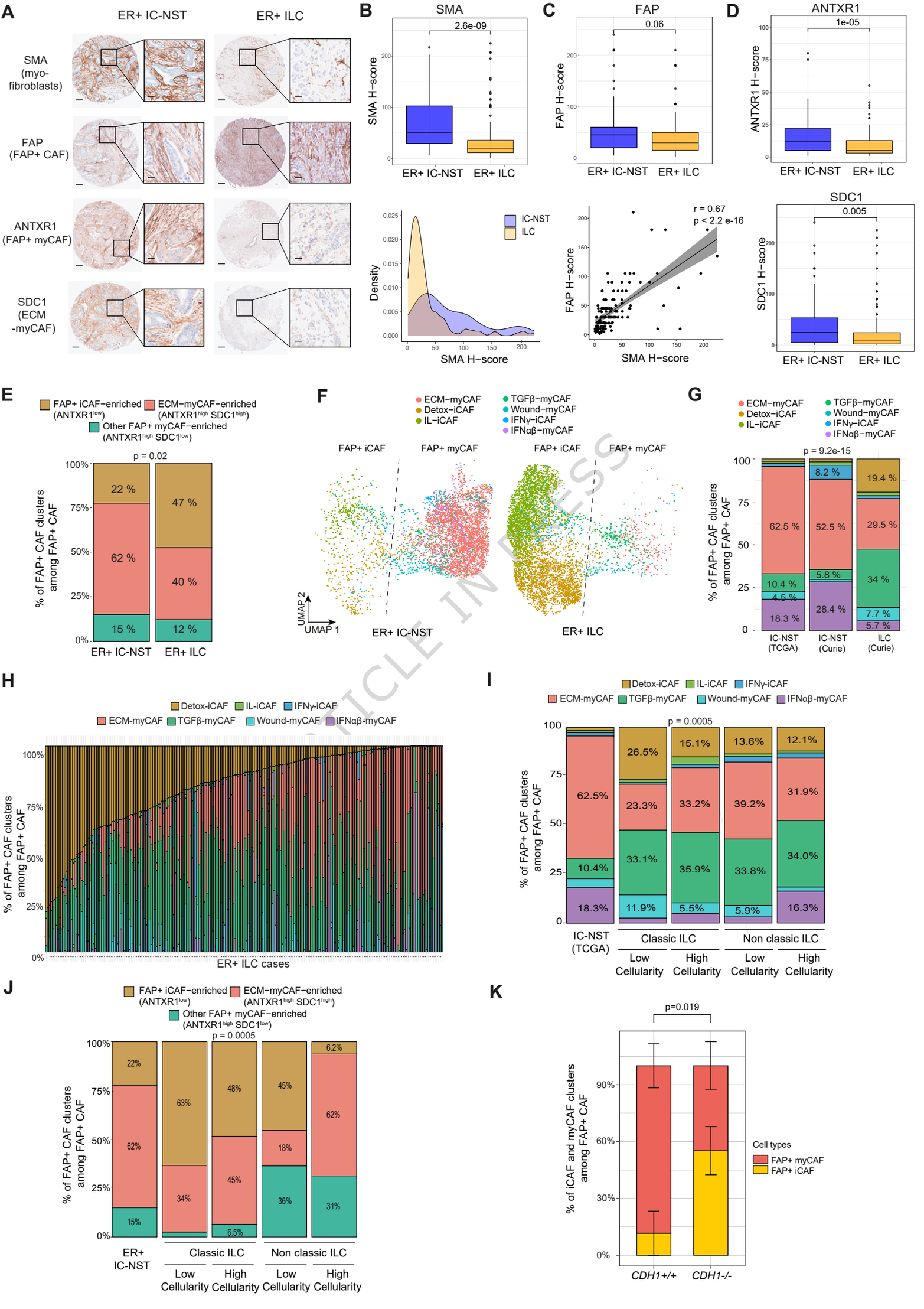

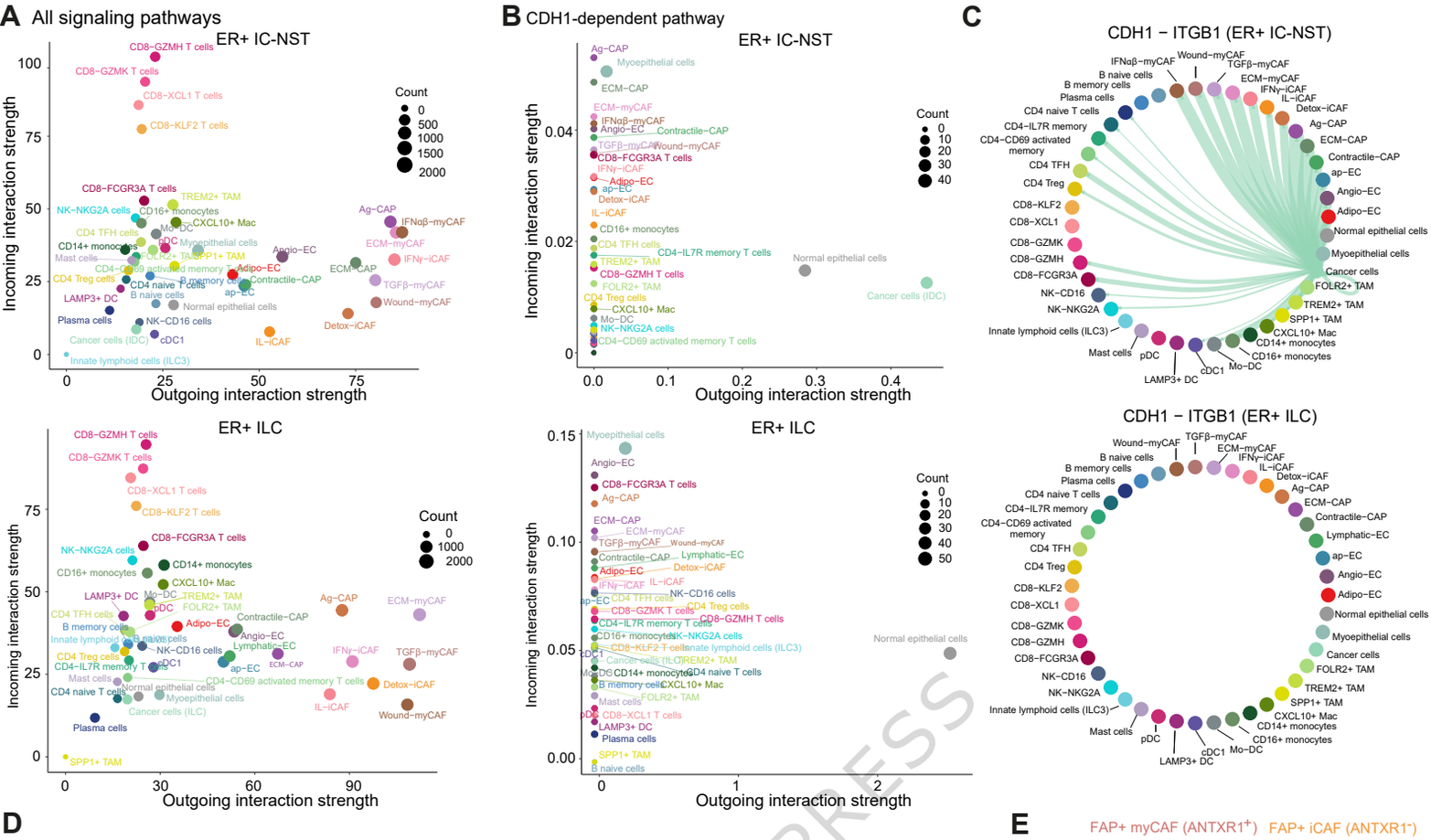
A All signaling pathways
ER+ IC-NST
Incoming interaction strength
Outgoing interaction strength
Count
ER+ ILC
B CDH1-dependent pathway
ER+ IC-NST
ER+ ILC
C
CDH1 − ITGB1 (ER+ IC-NST)
CDH1 − ITGB1 (ER+ ILC)

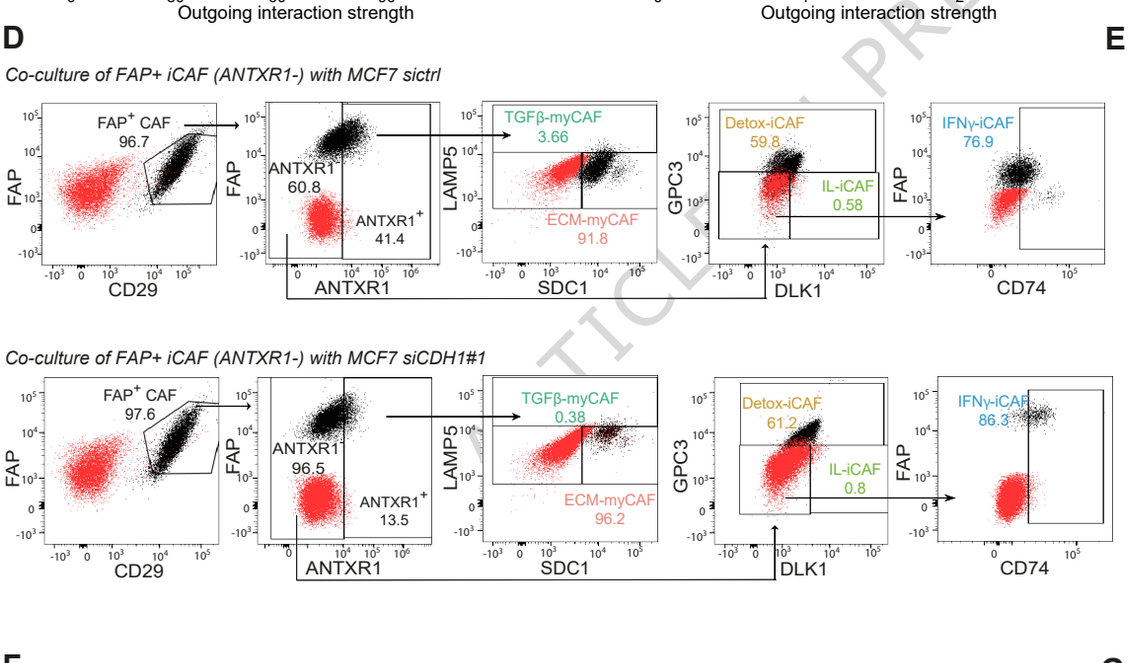
D
Co-culture of FAP+ iCAF (ANTXR1-) with MCF7 sictrl
FAP+ CAF 96.7
ANTXR1 60.8
ANTXR1+ 41.4
TGFβ-myCAF 3.66
ECM-myCAF 91.8
Detox-iCAF 59.8
IL-iCAF 0.58
IFNγ-iCAF 76.9
Co-culture of FAP+ iCAF (ANTXR1-) with MCF7 siCDH1#1
FAP+ CAF 97.6
ANTXR1 96.5
ANTXR1+ 13.5
TGFβ-myCAF 0.38
ECM-myCAF 96.2
Detox-iCAF 61.2
IL-iCAF 0.8
IFNγ-iCAF 86.3
CD29
ANTXR1
SDC1
DLK1
CD74

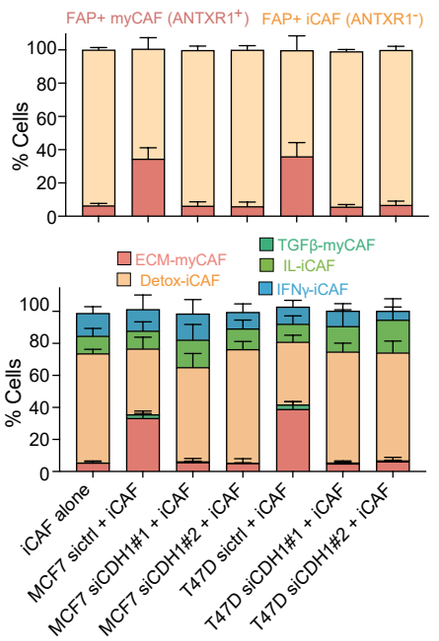
E
FAP+ myCAF (ANTXR1+)
FAP+ iCAF (ANTXR1-)
% Cells
ECM-myCAF
Detox-iCAF
TGFβ-myCAF
IL-iCAF
IFNγ-iCAF
iCAF alone
MCF7 sictrl + iCAF
MCF7 siCDH1#1 + iCAF
MCF7 siCDH1#2 + iCAF
T47D sictrl + iCAF
T47D siCDH1#1 + iCAF
T47D siCDH1#2 + iCAF

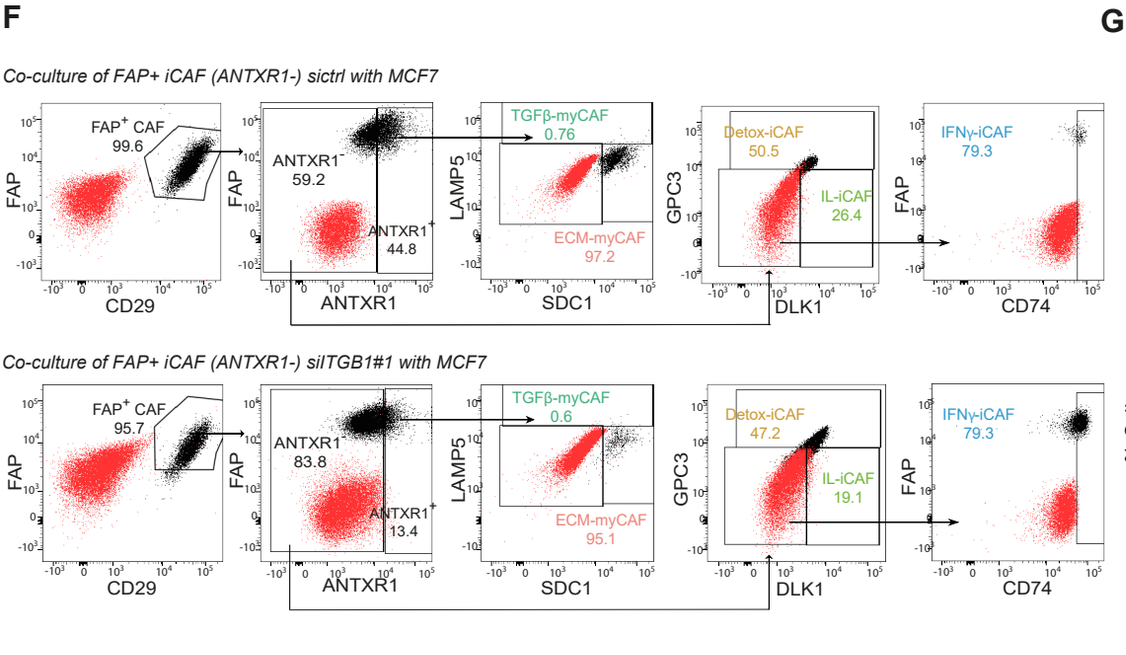
F
Co-culture of FAP+ iCAF (ANTXR1-) sictrl with MCF7
FAP+ CAF 99.6
ANTXR1- 59.2
ANTXR1+ 44.8
TGFβ-myCAF 0.76
ECM-myCAF 97.2
Detox-iCAF 50.5
IL-iCAF 26.4
IFNγ-iCAF 79.3
Co-culture of FAP+ iCAF (ANTXR1-) siITGB1#1 with MCF7
FAP+ CAF 95.7
ANTXR1 83.8
ANTXR1+ 13.4
TGFβ-myCAF 0.6
ECM-myCAF 95.1
Detox-iCAF 47.2
IL-iCAF 19.1
IFNγ-iCAF 79.3
CD29
ANTXR1
SDC1
DLK1
CD74

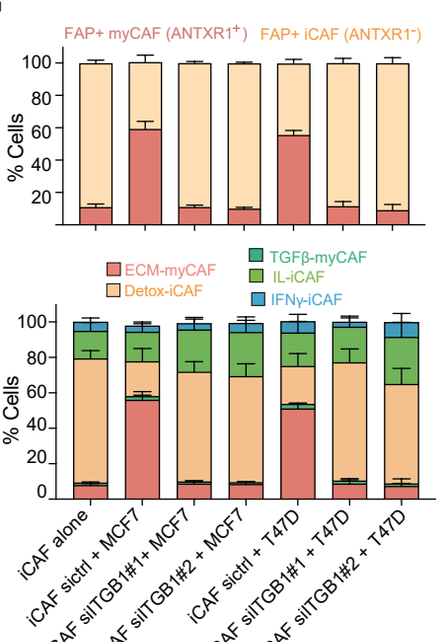
G
FAP+ myCAF (ANTXR1+)
FAP+ iCAF (ANTXR1-)
% Cells
ECM-myCAF
Detox-iCAF
TGFβ-myCAF
IL-iCAF
IFNγ-iCAF
iCAF alone
iCAF sictrl + MCF7
iCAF siITGB1#1+ MCF7
iCAF siITGB1#2 + MCF7
iCAF sictrl + T47D
iCAF siITGB1#1 + T47D
iCAF siITGB1#2 + T47D

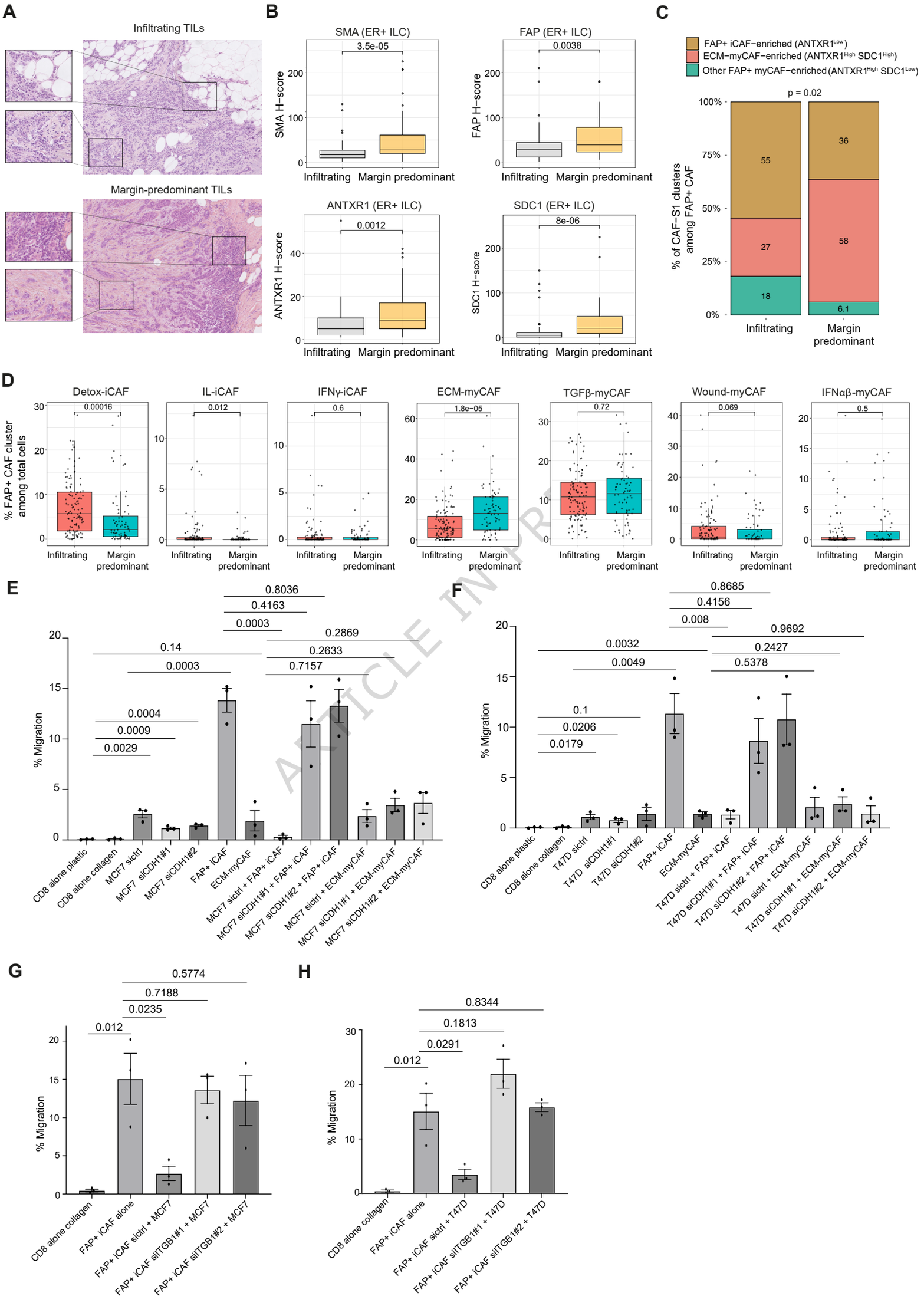
A
Infiltrating TILs
Margin-predominant TILs
B
SMA (ER+ ILC)
3.5e-05
SMA H−score
Infiltrating
Margin predominant
FAP (ER+ ILC)
0.0038
FAP H−score
ANTXR1 (ER+ ILC)
0.0012
ANTXR1 H−score
SDC1 (ER+ ILC)
8e-06
SDC1 H−score
C
FAP+ iCAF−enriched (ANTXR1Low)
ECM−myCAF−enriched (ANTXR1High SDC1High)
Other FAP+ myCAF−enriched (ANTXR1High SDC1Low)
p = 0.02
% of CAF−S1 clusters among FAP+ CAF
55
27
18
36
58
6.1
D
Detox-iCAF
0.00016
IL-iCAF
0.012
IFNγ-iCAF
0.6
ECM-myCAF
1.8e−05
TGFβ-myCAF
0.72
Wound-myCAF
0.069
IFNαβ-myCAF
0.5
% FAP+ CAF cluster among total cells
E
% Migration
0.8036
0.4163
0.0003
0.2869
0.14
0.2633
0.0003
0.7157
0.0004
0.0009
0.0029
CD8 alone plastic
CD8 alone collagen
MCF7 siCtrl
MCF7 siCDH1#1
MCF7 siCDH1#2
FAP+ iCAF
ECM-myCAF
MCF7 siCtrl + FAP+ iCAF
MCF7 siCDH1#1 + FAP+ iCAF
MCF7 siCDH1#2 + FAP+ iCAF
MCF7 siCtrl + ECM-myCAF
MCF7 siCDH1#1 + ECM-myCAF
MCF7 siCDH1#2 + ECM-myCAF
F
% Migration
0.8685
0.4156
0.008
0.9692
0.0032
0.2427
0.0049
0.5378
0.1
0.0206
0.0179
CD8 alone plastic
CD8 alone collagen
T47D siCtrl
T47D siCDH1#1
T47D siCDH1#2
FAP+ iCAF
ECM-myCAF
T47D siCtrl + FAP+ iCAF
T47D siCDH1#1 + FAP+ iCAF
T47D siCDH1#2 + FAP+ iCAF
T47D siCtrl + ECM-myCAF
T47D siCDH1#1 + ECM-myCAF
T47D siCDH1#2 + ECM-myCAF
G
% Migration
0.5774
0.7188
0.0235
0.012
CD8 alone collagen
FAP+ iCAF alone
FAP+ iCAF siCtrl + MCF7
FAP+ iCAF siITGB1#1 + MCF7
FAP+ iCAF siITGB1#2 + MCF7
H
% Migration
0.8344
0.1813
0.0291
0.012
CD8 alone collagen
FAP+ iCAF alone
FAP+ iCAF siCtrl + T47D
FAP+ iCAF siITGB1#1 + T47D
FAP+ iCAF siITGB1#2 + T47D

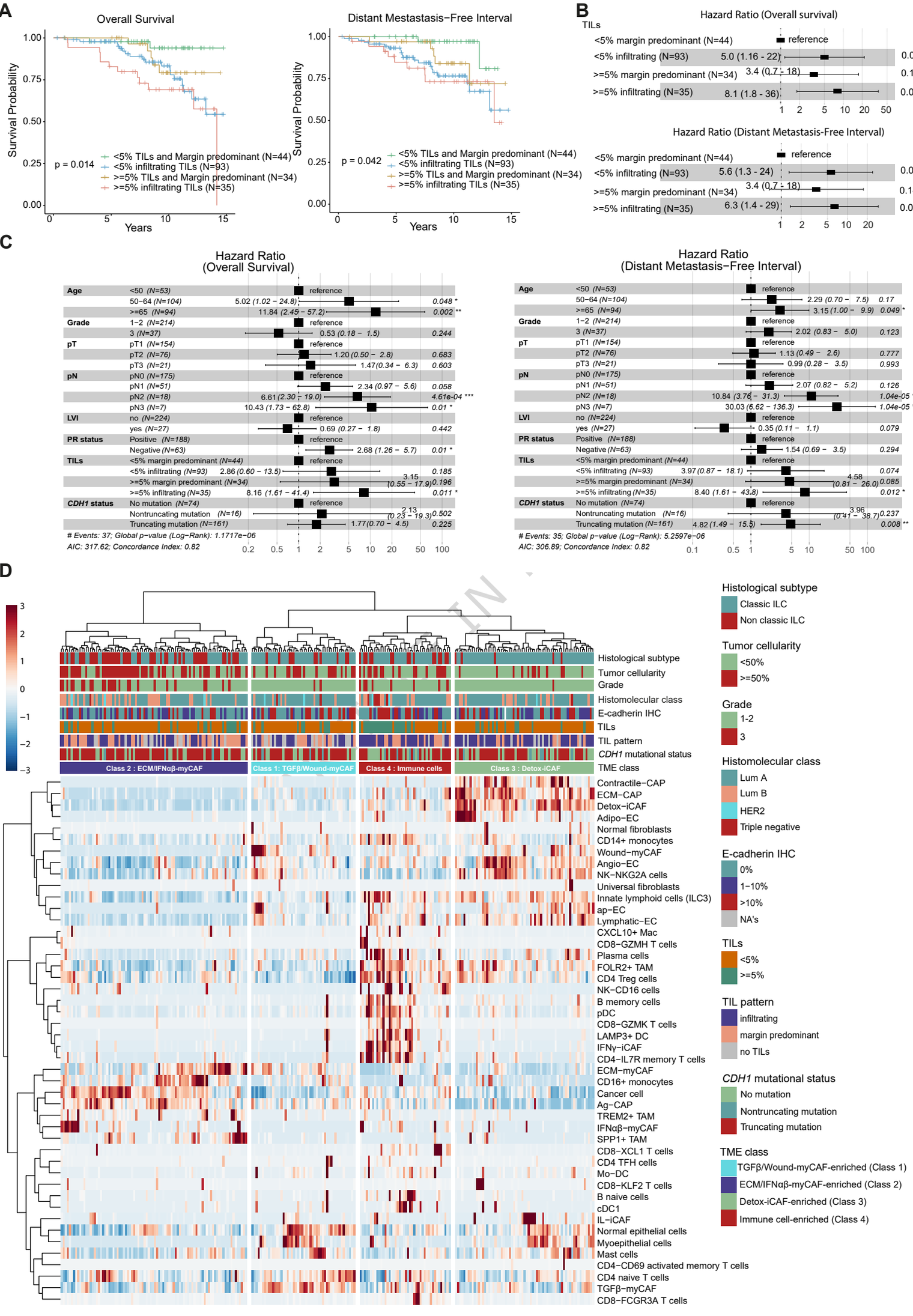
A
Overall Survival
Survival Probability
p = 0.014
<5% TILs and Margin predominant (N=44)
<5% infiltrating TILs (N=93)
>=5% TILs and Margin predominant (N=34)
>=5% infiltrating TILs (N=35)
Years
Distant Mestastasis−Free Interval
p = 0.042
B
Hazard Ratio (Overall survival)
TILs
<5% margin predominant (N=44) reference
<5% infiltrating (N=93) 5.0 (1.16 - 22) 0.031 *
>=5% margin predominant (N=34) 3.4 (0.7 - 18) 0.144
>=5% infiltrating (N=35) 8.1 (1.8 - 36) 0.006 **
Hazard Ratio (Distant Metastasis-Free Interval)
<5% infiltrating (N=93) 5.6 (1.3 - 24) 0.02 *
>=5% infiltrating (N=35) 6.3 (1.4 - 29) 0.018 *
C
Hazard Ratio
(Overall Survival)
Age <50 (N=53) reference
50−64 (N=104) 5.02 (1.02 − 24.8) 0.048 *
>=65 (N=94) 11.84 (2.45 − 57.2) 0.002 **
Grade 1−2 (N=214) reference
3 (N=37) 0.53 (0.18 − 1.5) 0.244
pT pT1 (N=154) reference
pT2 (N=76) 1.20 (0.50 − 2.8) 0.683
pT3 (N=21) 1.47 (0.34 − 6.3) 0.603
pN pN0 (N=175) reference
pN1 (N=51) 2.34 (0.97 − 5.6) 0.058
pN2 (N=18) 6.61 (2.30 − 19.0) 4.61e-04 ***
pN3 (N=7) 10.43 (1.73 − 62.8) 0.01 *
LVI no (N=224) reference
yes (N=27) 0.69 (0.27 − 1.8) 0.442
PR status Positive (N=188) reference
Negative (N=63) 2.68 (1.26 − 5.7) 0.01 *
TILs <5% margin predominant (N=44) reference
<5% infiltrating (N=93) 2.86 (0.60 − 13.5) 0.185
>=5% margin predominant (N=34) 3.15 (0.55 − 17.9) 0.196
>=5% infiltrating (N=35) 8.16 (1.61 − 41.4) 0.011 *
CDH1 status No mutation (N=74) reference
Nontruncating mutation (N=16) 2.13 (0.23 − 19.3) 0.502
Truncating mutation (N=161) 1.77 (0.70 − 4.5) 0.225
Events: 37; Global p−value (Log−Rank): 1.1717e−06
AIC: 317.62; Concordance Index: 0.82
Hazard Ratio
(Distant Metastasis−Free Interval)
Age <50 (N=53) reference
50−64 (N=104) 2.29 (0.70 − 7.5) 0.17
>=65 (N=94) 3.15 (1.00 − 9.9) 0.049 *
Grade 1−2 (N=214) reference
3 (N=37) 2.02 (0.83 − 5.0) 0.123
pT pT1 (N=154) reference
pT2 (N=76) 1.13 (0.49 − 2.6) 0.777
pT3 (N=21) 0.99 (0.28 − 3.5) 0.993
pN pN0 (N=175) reference
pN1 (N=51) 2.07 (0.82 − 5.2) 0.126
pN2 (N=18) 10.84 (3.76 − 31.3) 1.04e-05 ***
pN3 (N=7) 30.03 (5.62 − 136.3) 1.04e-05 ***
LVI no (N=224) reference
yes (N=27) 0.35 (0.11 − 1.1) 0.079
PR status Positive (N=188) reference
Negative (N=63) 1.54 (0.69 − 3.5) 0.294
TILs <5% margin predominant (N=44) reference
<5% infiltrating (N=93) 3.97 (0.87 − 18.1) 0.074
>=5% margin predominant (N=34) 4.58 (0.81 − 26.0) 0.085
>=5% infiltrating (N=35) 8.40 (1.61 − 43.8) 0.012 *
CDH1 status No mutation (N=74) reference
Nontruncating mutation (N=16) 3.96 (0.41 − 38.7) 0.237
Truncating mutation (N=161) 4.82 (1.49 − 15.5) 0.008 **
Events: 35; Global p−value (Log−Rank): 5.2597e−06
AIC: 306.89; Concordance Index: 0.82
D
Histological subtype
Tumor cellularity
Grade
Histomolecular class
E-cadherin IHC
TILs
TIL pattern
CDH1 mutational status
TME class
Class 2 : ECM/IFNαβ-myCAF
Class 1: TGFβ/Wound-myCAF
Class 4 : Immune cells
Class 3 : Detox-iCAF
Contractile−CAP
ECM−CAP
Detox−iCAF
Adipo−EC
Normal fibroblasts
CD14+ monocytes
Wound−myCAF
Angio−EC
NK−NKG2A cells
Universal fibroblasts
Innate lymphoid cells (ILC3)
ap−EC
Lymphatic−EC
CXCL10+ Mac
CD8−GZMH T cells
Plasma cells
FOLR2+ TAM
CD4 Treg cells
NK−CD16 cells
B memory cells
pDC
CD8−GZMK T cells
LAMP3+ DC
IFNγ−iCAF
CD4−IL7R memory T cells
ECM−myCAF
CD16+ monocytes
Cancer cell
Ag−CAP
TREM2+ TAM
IFNαβ−myCAF
SPP1+ TAM
CD8−XCL1 T cells
CD4 TFH cells
Mo−DC
CD8−KLF2 T cells
B naive cells
cDC1
IL−iCAF
Normal epithelial cells
Myoepithelial cells
Mast cells
CD4−CD69 activated memory T cells
CD4 naive T cells
TGFβ−myCAF
CD8−FCGR3A T cells
Histological subtype
Classic ILC
Non classic ILC
Tumor cellularity
<50%
>=50%
Grade
1-2
3
Histomolecular class
Lum A
Lum B
HER2
Triple negative
E-cadherin IHC
0%
1−10%
>10%
NA's
TILs
<5%
>=5%
TIL pattern
infiltrating
margin predominant
no TILs
CDH1 mutational status
No mutation
Nontruncating mutation
Truncating mutation
TME class
TGFβ/Wound-myCAF-enriched (Class 1)
ECM/IFNαβ-myCAF-enriched (Class 2)
Detox-iCAF-enriched (Class 3)
Immune cell-enriched (Class 4)

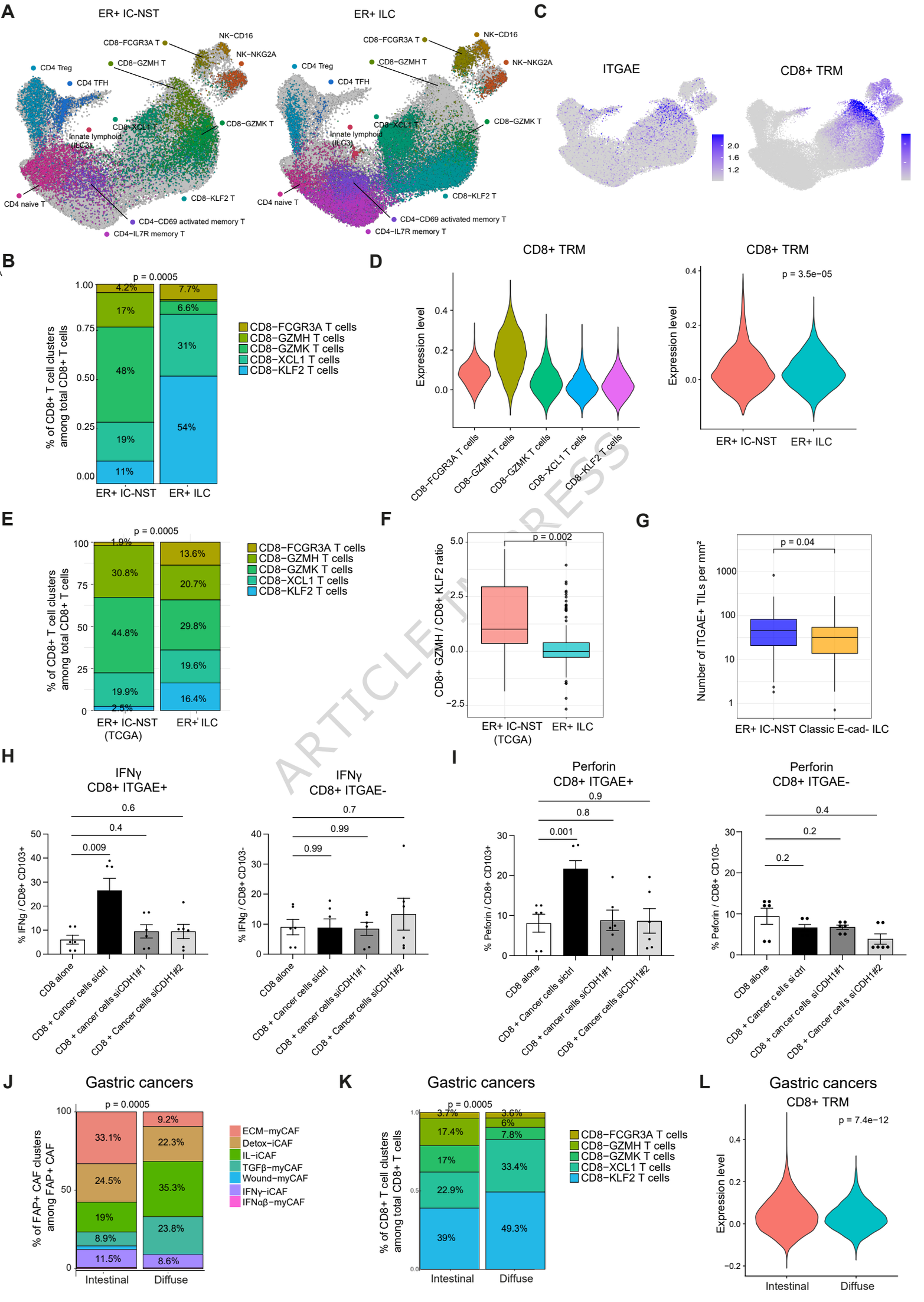

A

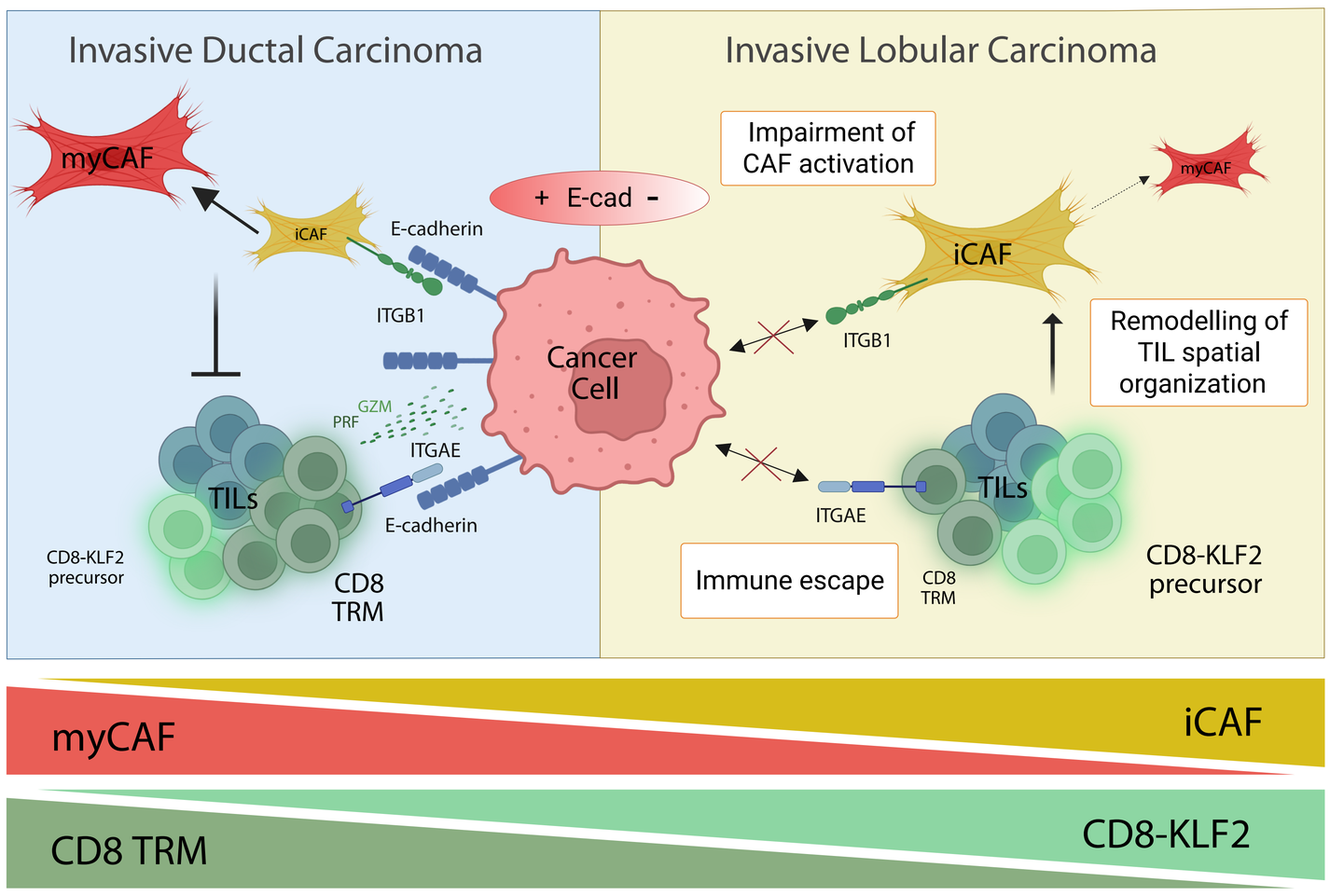

B